



## **Summer School Project DESY 2012**

### **Performance study of the Datura pixel beam telescope at DESY test beam.**

Mateusz Dominiak, AGH University of Science and Technology, Poland

September 07, 2012

#### **Abstract**

The following report presents resolution study of the Datura pixel beam telescope. The data used in this study, was taken in test beam area 21 at DESY with positron beam. The main goal of this project is to determine resolution of the telescope for different setup settings and find the most optimal one.

# Contents

<b>1</b>	<b>Introduction</b>	<b>3</b>
<b>2</b>	<b>The Datura Telescope</b>	<b>3</b>
2.1	The hardware overview . . . . .	3
2.2	Mimosa26 . . . . .	4
<b>3</b>	<b>Measurements</b>	<b>5</b>
3.1	Test beam at DESY . . . . .	5
<b>4</b>	<b>The Offline Analysis</b>	<b>5</b>
4.1	Reconstruction of the tracks . . . . .	5
4.2	Noise occupancy . . . . .	6
4.3	Average cluster size . . . . .	7
4.4	Efficiency of the cluster finding . . . . .	8
4.5	Residuals distribution . . . . .	9
4.6	Intrinsic resolution of Mimosa26 . . . . .	10
<b>5</b>	<b>Results</b>	<b>12</b>
<b>6</b>	<b>Summary</b>	<b>14</b>
	<b>Bibliography</b>	<b>15</b>
<b>A</b>	<b>Residuals distributions</b>	<b>16</b>
<b>B</b>	<b>Fitted widths of unbiased residuals</b>	<b>30</b>
<b>C</b>	<b>Efficiency and resolution plots</b>	<b>35</b>

# 1 Introduction

The parameter which is going to be under studies, is a threshold at the discriminator on Mimosa26 sensors. In order to do that the data was taken with different threshold settings from 3 up to 12, in dimensionless signal-to-noise ratio values.

Each data sample consists of  $10^5$  events and they were taken with three different beam energies: 2, 3, 5 GeV.

The geometry setup of the telescope was 20 mm distance between each sensor plane.

The section no. 2 describes briefly the telescope and its hardware components. Next section no. 3 characterizes conditions where data was taken. Further section no. 4 shows analysis done during this project and how the results have been obtained. The last section no. 5 summarizes the work which was done and presents final results.

It is worth mentioning that similar studies has been partially done in the past on the telescope Aconite which is situated at CERN, with the test beam energy of 120 GeV [9].

## 2 The Datura Telescope

The telescope is equipped in two arms with three sensors on each of it, as it can be seen on the Fig. 1. The main purpose of the telescope is to provide trajectory of the passing particles through the telescope with very good precision. This feature allows studying properties of the new detectors and monitor its performance. To perform studies as precise as possible it is essential to understand its behavior and evaluate most optimal settings of its usage. To improve performance of the telescope, the following study has been done.

### 2.1 The hardware overview

The main components of the telescope are:

- $6 \times$  Mimosa26 sensors
- Trigger logic unit - (Fig. 2)
- Telescope Photomultipliers tubes (PMT)
- Power supply - (Fig. 2)
- Cooling system
- National Instruments crate - (Fig. 2)

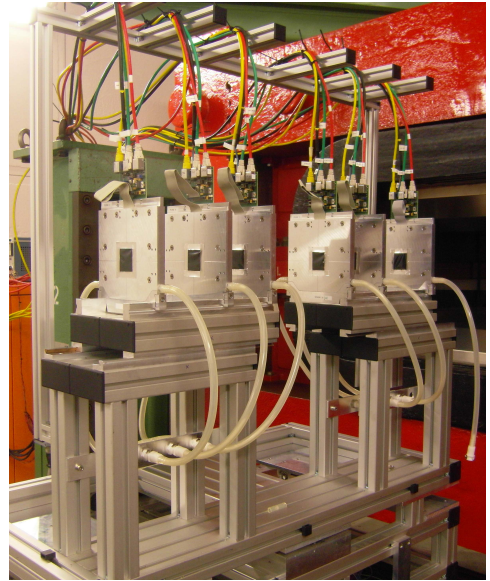


Figure 1: *Picture of the Datura Telescope*

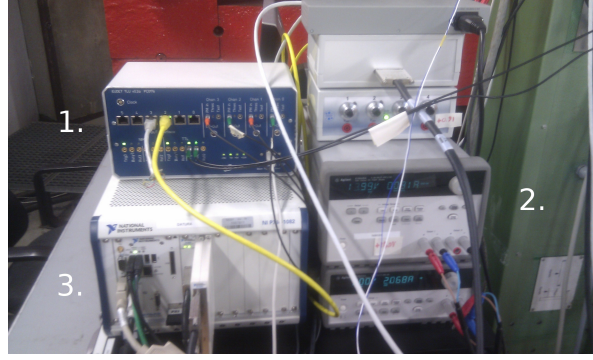


Figure 2: *Picture of the readout equipment in test beam 21 area, components are explained by labels: 1) Trigger logic unit, 2) Power supply, 3) National Instruments crate*

The Fig. 3 presents logical scheme of the EUDET telescope and its assembly.

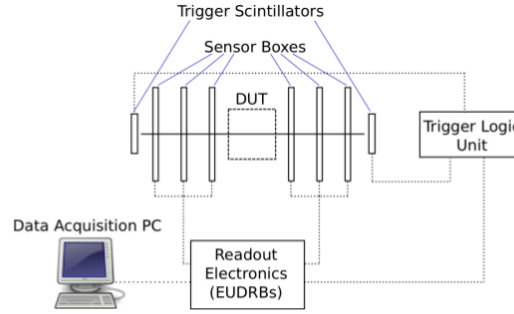


Figure 3: *Configuration sketch*

## 2.2 Mimosa26

is a monolithic active pixel sensor (MAPS), it is fabricated in CMOS technology, the thickness of the sensor is  $50 \mu m$ . It has 1152 columns and 576 rows, with pitch size  $18.4 \mu m$ , which is equal to active area of  $2 cm^2$ . Mimosa26 is designed to work at room temperatures. Mimosa26 has binary readout and can run with clock frequency up to 80 MHz, this provides low track multiplicity level per frame. Each pixel is equipped with amplifier and correlated double sampling (CDS), at the end of each column is placed discriminator.

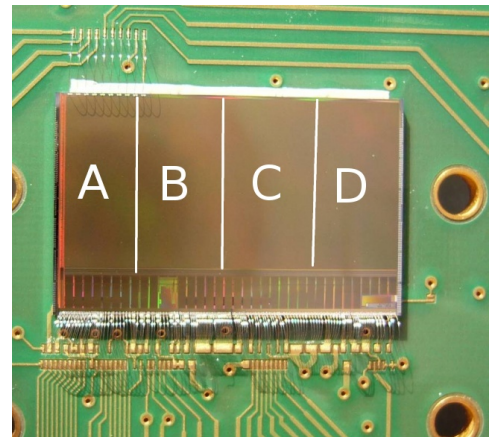


Figure 4: *The photography of the Mimosa26 sensor on a PCB with section numbering used in this paper [4].*



### 3 Measurements

DESY provides three test beam lines (21, 22 and 24). These electron or positron beams are converted bremsstrahlung beams from carbon fibre targets in the lepton synchrotron DESY II with up to 1000 particles per  $cm^2$  and second, energies from 1 to 6 GeV, an energy spread of 5% and a divergence of 2 mrad[6].

#### 3.1 Test beam at DESY

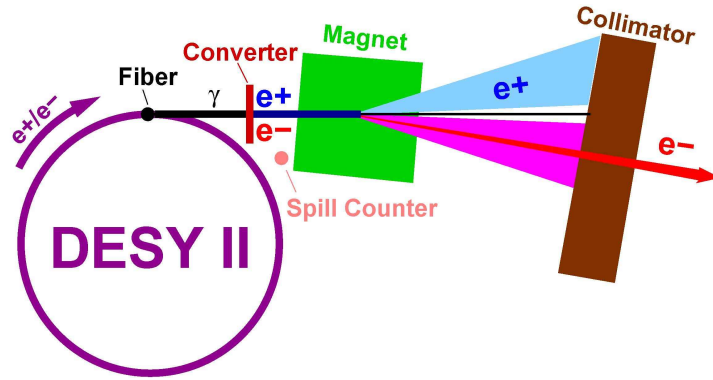


Figure 5: *Scheme of the test beam production at DESY II*

To perform noise studies data was taken separately with absence of the test beam. Sensors were cooled to the temperature of 10 degrees.

### 4 The Offline Analysis

#### 4.1 Reconstruction of the tracks

is split into following steps:

- Conversion
- Clustering
- Hitmaker
- Alignment
- Track fitting

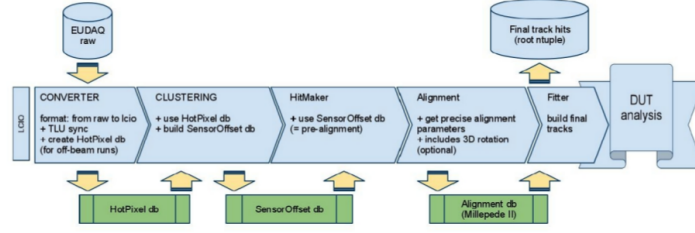


Figure 6: *Data flow of the analysis steps.*

The full scheme of reconstruction steps can be seen on the figure below.

Due to huge time consumption of the reconstruction procedure, the following analysis has been performed with only  $10^4$  reconstructed events.

In active sensor area we can distinguish four regions, each region can behave differently from each other. To perform studies more precisely every section of the sensor was under investigation separately and the following study is presented for section *A*. The numeration of the section can be seen in the picture 4.

## 4.2 Noise occupancy

The first step of study was analysis of the noise in Mimosa26 sensors. Fluctuations in the pixel circuit in the sensor can be strong enough to spontaneously fire pixel. If pixel fires or does not, decides a threshold level at the discriminator.

Noise occupancy can be defined as a ratio of pixels firing due to noise to number of pixels situated in the section.

$$\text{Noise occupancy} = \frac{\text{Average number of firing pixels per event}}{\text{Number of pixels in the section}}$$

where number of pixels in the section equals 165888.

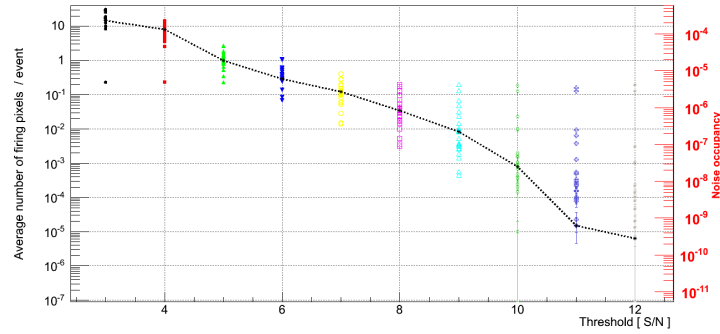


Figure 7: *Noise occupancy of the Mimosa26 sensors*

As can be seen on Fig. 7 there is very strong dependence on the threshold level and noise occupancy, to illustrate this relation, the black line has been drawn which connects the measurements coming from the same section, on one of the sensors.

### 4.3 Average cluster size

To present how distribution of the cluster size is varying with the threshold level the Figs. 8a and 8b have been plotted for the lowest, middle and highest threshold level. Histograms have been normalized thus each bin represents a probability of the appearance such a cluster size for corresponding threshold level.

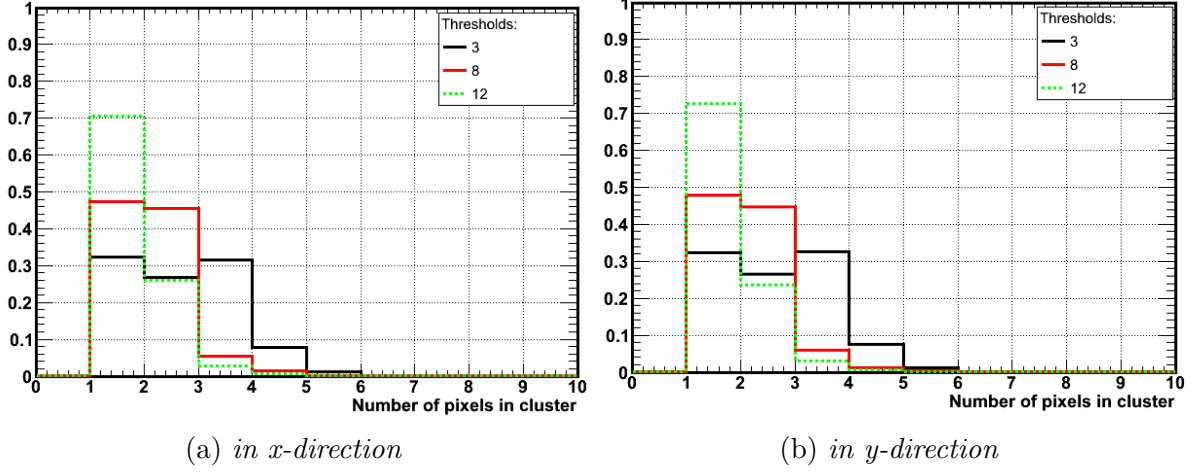


Figure 8: Cluster size at the sensor no. 76 (plane 2)

The Figures 9a and 9b present mean cluster size for section A in  $x$ - and  $y$ -directions respectively.

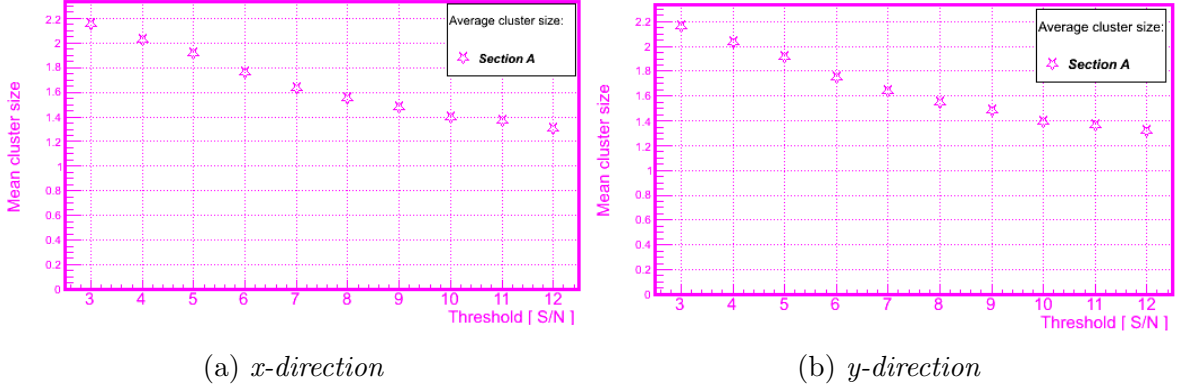


Figure 9: Average cluster size at the sensor no. 76 (plane 2)

At the figure below can be seen comparison of the mean cluster size of the matched clusters to the tracks (*right plot*), and all clusters (*left plot*).

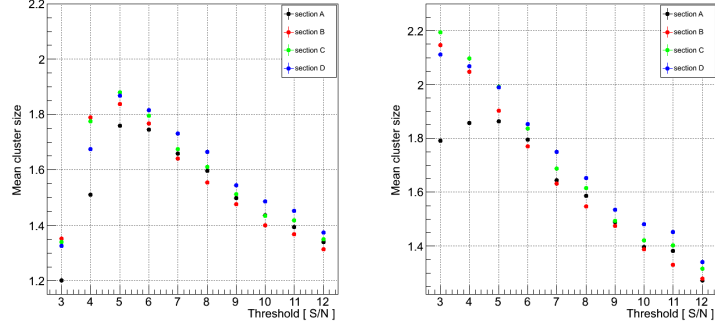


Figure 10: *Average cluster size at the sensor no. 76 (plane 2)*

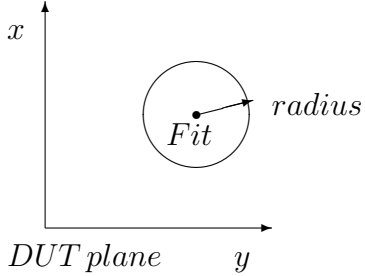
As it is foreseen the average cluster size of matched clusters for lower threshold increases due to suppression of bigger fraction of small clusters which come from noise.

#### 4.4 Efficiency of the cluster finding

can be described as ratio of the matched hits in the DUT to the tracks to the whole number of the tracks.

$$\varepsilon_{ff} = \frac{N_{hit}}{N_{track}}$$

Track fit is extrapolated through the DUT plane and in certain radius (in this study it is  $50 \mu m$ ) from track fit position on the DUT plane, is being searched for clusters.



The errors are calculated in the following way, the probability that assigned hit to track fit comes from noise can be calculated as a number of pixels in area where it is looking for hits multiplied by noise occupancy.

Error bars are not visible in the figure due to its very small size.

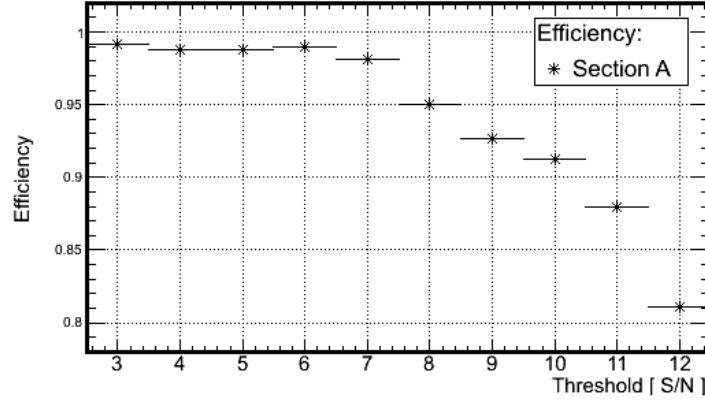


Figure 11: *Efficiency at the sensor no. 76 (plane 2), beam energy 2 GeV*

There is significant drop in cluster finding efficiency in higher threshold level than 7 S/N, due to suppression signal coming from particles.

To show how efficiency affects the performance of the track reconstruction the Fig. 12 shows track rate per event in reconstructed  $10^4$  events for different threshold level and beam energy. As it can be seen the track multiplicity has the highest value for the low thresholds and beam energy 2 and 3 GeV, for the beam energy 5 GeV this dependency is not so significant.

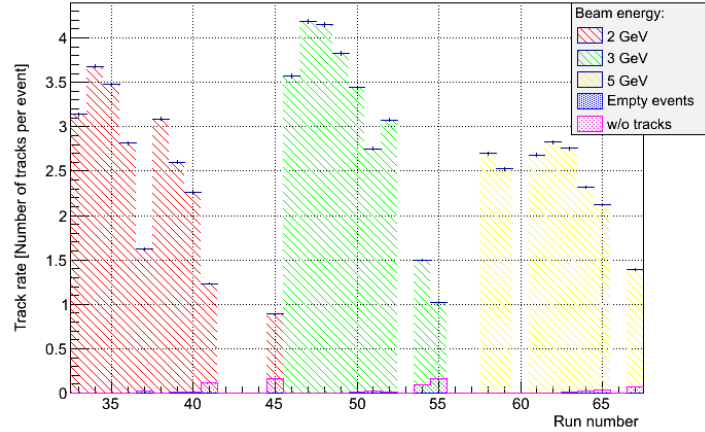


Figure 12: *Track rate; threshold level increases with run number for each beam energy respectively.*

## 4.5 Residuals distribution

The first step of the analysis is to determine the width of the residuals distribution. With very close approximation it can be assumed that these distributions (without tails) are Gaussian like.

As an example, the distributions have been drawn for threshold 3 in figures 13a and 13b, separately for each sensor plane in  $x$ - and  $y$ -direction.

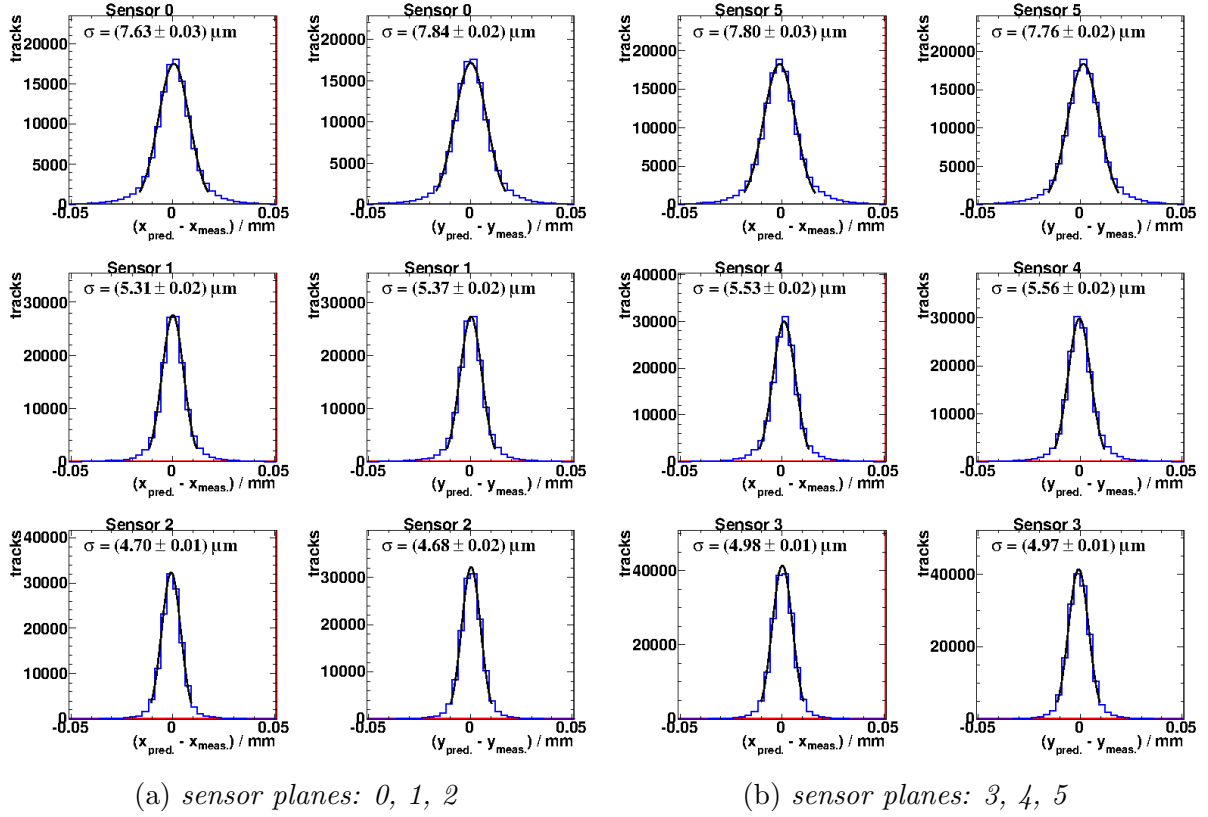


Figure 13: *Residuals distributions, beam energy 2 GeV [8]*

## 4.6 Intrinsic resolution of Mimosa26

The width of the residuals distribution is denoted as  $\sigma_{tot.}$  in equation 1. In the same equation  $\sigma_{tel.}$  is a telescope pointing resolution and  $\sigma_{DUT}$  is a reference plane intrinsic resolution.

$$\sigma_{tot.}^2 = \sigma_{tel.}^2 + \sigma_{DUT}^2 \quad (1)$$

To obtain intrinsic resolution of the Mimosa26 sensors the following steps have been done.

In the Fig. 14 there are drawn widths ( $\sigma_{tot.}$ ) of the residuals distributions for for each sensor plane as a function of distance in perpendicular direction from sensor plane 0. Each sensor plane has the same intrinsic resolution, parameterizing previous equation into equation 2, where the free parameter is intrinsic resolution ( $\sigma_{DUT}$ ), it is possible to extract that value from the fit.

$$\sigma_{tot.}^2 = f(\sigma_{DUT}) \quad (2)$$

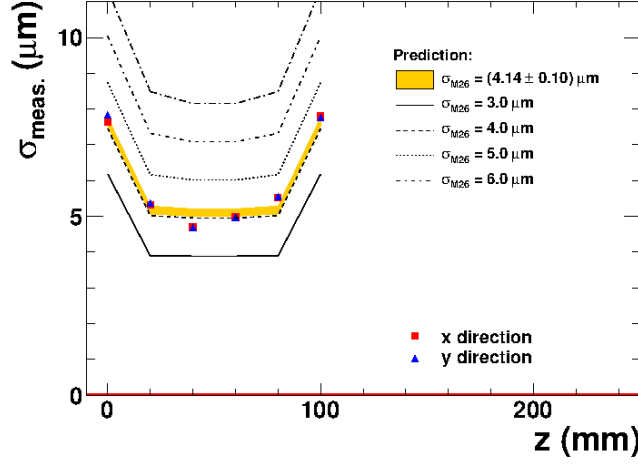


Figure 14: *Fitted widths of the unbiased residuals as a function of distance, beam energy 2 GeV.[8]*

The minimization of the  $\chi^2$  fit leads to the most accurate intrinsic resolution as a result. The  $\chi^2$  function can be split into two components, coming from  $x$ - and  $y$ -direction measurements respectively.

$$\chi^2 = \chi_x^2 + \chi_y^2 \quad (3)$$

Each component of the equation 3 has contribution coming from position and scattering angle measurement, which can be expressed as a two sums, in terms of the sensor intrinsic resolution ( $\sigma_s$ ) and scattering angel ( $\sigma_\theta$ ) respectively, what can be seen in equation below.

$$\chi_x^2 = \sum_{i=1}^N \left( \frac{x_{meas.}^i - x_{fit}^i}{\sigma_s} \right)^2 + \sum_{i=2}^{N-1} \left( \frac{\theta_x^i - \theta_x^{i-1}}{\sigma_\theta^i} \right)^2 \quad (4)$$

where  $x_{meas.}^i$  is a  $x$  component of the position measurement,  $x_{fit}^i$  is a  $x$  coordinate of the fitted track and  $\theta_x^i$  is a scattered angel, for plane number  $i$ .

Formula for  $\chi_y^2$  can be obtained analogously from equation 4.

Expected multiple scattering angel can be calculated from equation 5 which takes into account thickness of the sensor ( $d = 50 \mu m$ ), material it is made of, in radiation length units ( $X_0 \approx 13.6 mm$  for silicon) and momentum of the particle.

$$\sigma_\theta = \frac{13.6 MeV}{\beta c p} \sqrt{\frac{d}{X_0}} \left[ 1 + 0.038 \ln \left( \frac{d}{X_0} \right) \right] \quad (5)$$



## 5 Results

Result of the repetition just mentioned procedure for every data sample with different threshold level can be seen in the Fig. 15, which presents combination of the telescope pointing resolution, intrinsic mimosa resolution and unbiased residuals distribution for section A.

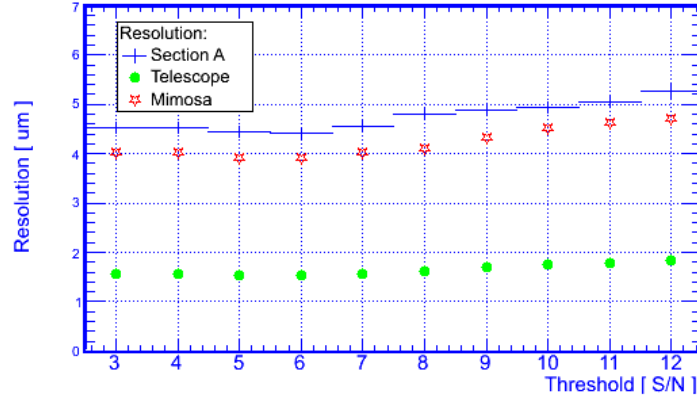


Figure 15: *Plane 2 (sensor no.76): unbiased residuals extracted from Figs. 13a and 13b plots, and Mimosa26 intrinsic resolution and telescope pointing resolution, beam energy 2 GeV.*

Measured dependency of the intrinsic Mimosa26 resolution on the threshold level, does not reflect the theoretical prediction.

To show how cluster size affects the resolution the following plot presents the width of the residuals distribution in  $x$ -direction.

Bins for higher cluster size are not visible on this plot because of its values reaching much further then range on axis.

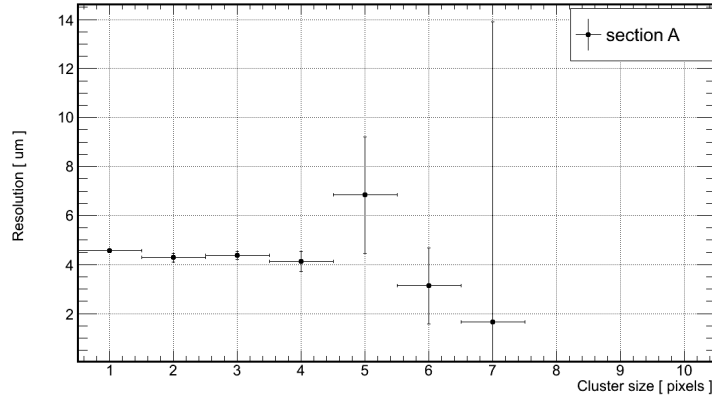


Figure 16: *Unbiased residuals as a function of cluster size for sensor plane 2, threshold level 3 and beam energy 2 GeV.*

In this study the following conclusions were evaluated. Telescope pointing resolution does not depend on average cluster size. Intrinsic Mimosa26 resolution depends on beam energy what is not with the agreement of the theoretical prediction. Moreover intrinsic resolution depends on average cluster size, what is in this case foreseen.

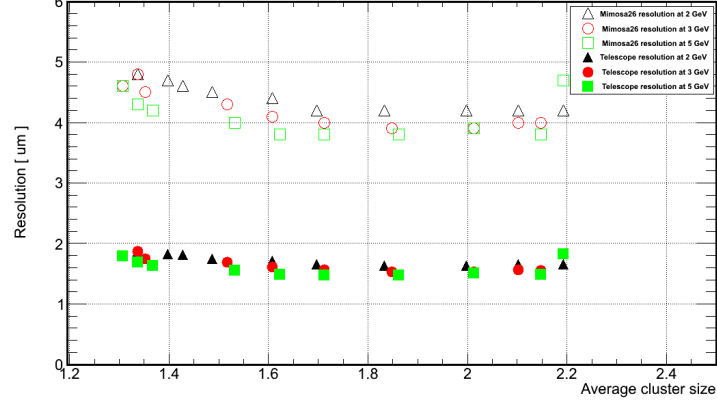


Figure 17: *Intrinsic resolution of Mimosa26 and pointing resolution of the telescope (at plane 2) as a function of the average cluster size.*

The extrapolation of the intrinsic Mimosa26 resolution (to cluster size 1) should lead to the peaking value  $\frac{18.4}{\sqrt{12}} \mu m$ , which is variation of the flat distribution.

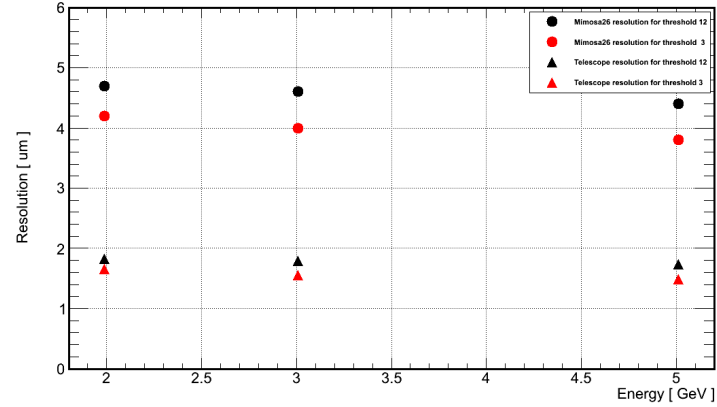


Figure 18: *Intrinsic resolution of the Mimosa26 and pointing resolution of the telescope as a function of the energy.*

The three points of the telescope pointing resolution obtained for the threshold 8 are included into plot below. As it can be seen they do not agree with theoretical line which corresponds to telescope geometry at which data was taken (20 mm between sensor planes).

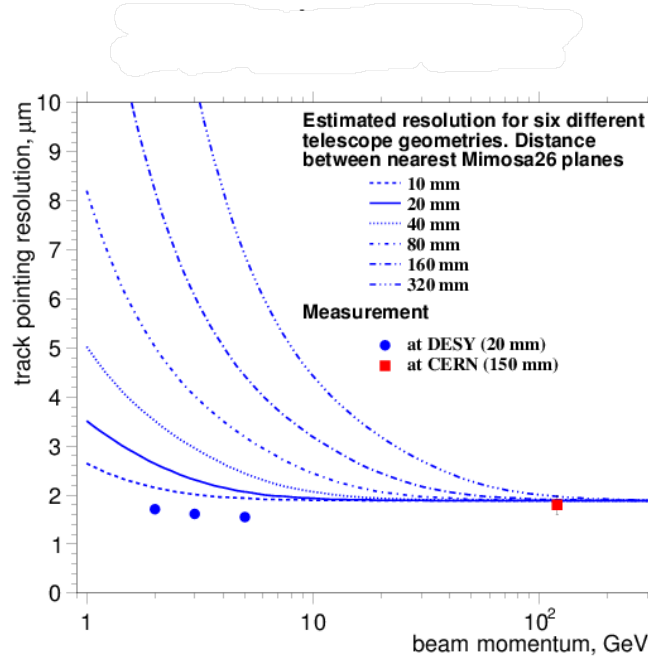


Figure 19: *Estimated and measured resolution for equidistant setup with 6 planes [8]*

Error bars due to its size are not seen.

## 6 Summary

These results should lead to further investigation of the behavior of the Mimosa26 sensors in context of the threshold level, in order to improve theoretical model how the sensors work.

There has been established that one of the most optimal setting for the Mimosa26 sensors is threshold level 6 or 7.

As it was mentioned at the beginning the similar study has been partially done in the past on the telescope *Aconite* which is situated at CERN, with the test beam energy of 120 GeV and this study was a extension of the previously obtained results [9].

## Acknowledgements

*I would like to thank my supervisor Dr Igor Rubinskiy for his support and tremendous help during this summer school project.*

*Moreover I would like to express my sincerest thanks to Marcel Stanitzki, Ingrid-Maria Gregor and whole ATLAS group as well.*

## References

- [1] Semiconductor Radiation Detectors  
*Dr. Gerhard Lutz, 1999, Semiconductor Laboratory of the Max-Planck-Institutes for Physics and Extraterrestrial Physics*
- [2] Revised January 2012 by H. Bichsel (University of Washington), D.E. Groom (LBNL), and S.R. Klein (LBNL). *PASSAGE OF PARTICLES THROUGH MATTER*
- [3] J. Beringer et al.(PDG), PR D86, 010001 (2012). *PARTICLE DETECTORS AT ACCELERATORS*
- [4] Picture of Mimosa26 sensor <http://www.iphc.cnrs.fr/Pictures-of-Mimosa-chips.html>
- [5] A.F. Zarnecki and P. Niezurawski, EUDET telescope geometry and resolution studies, EUDET-Report-2007-01, arXiv:physics/0703058. *A.F.Zarnecki , P.Niezurawski*
- [6] <http://adweb.desy.de/home/testbeam/WWW/Description.html>
- [7] EU Telescope. Offline track reconstruction and DUT analysis software. *Igor Rubinskiy December 1, 2010*
- [8] Code used to generate the plots with permission of I. Rubinskiy, private communication, 2012
- [9] Silvan Kuttimalai, 2011, Resolution Measurements With the Eudet Pixel Telescope

## A Residuals distributions

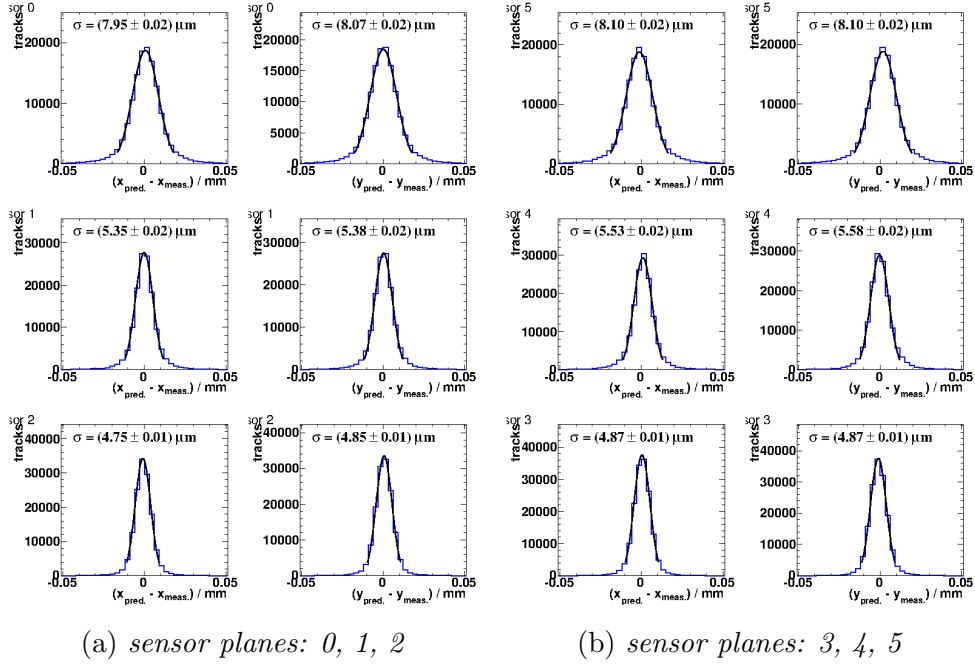


Figure 20: *Residuals distributions for threshold 4 and beam energy 2 GeV*

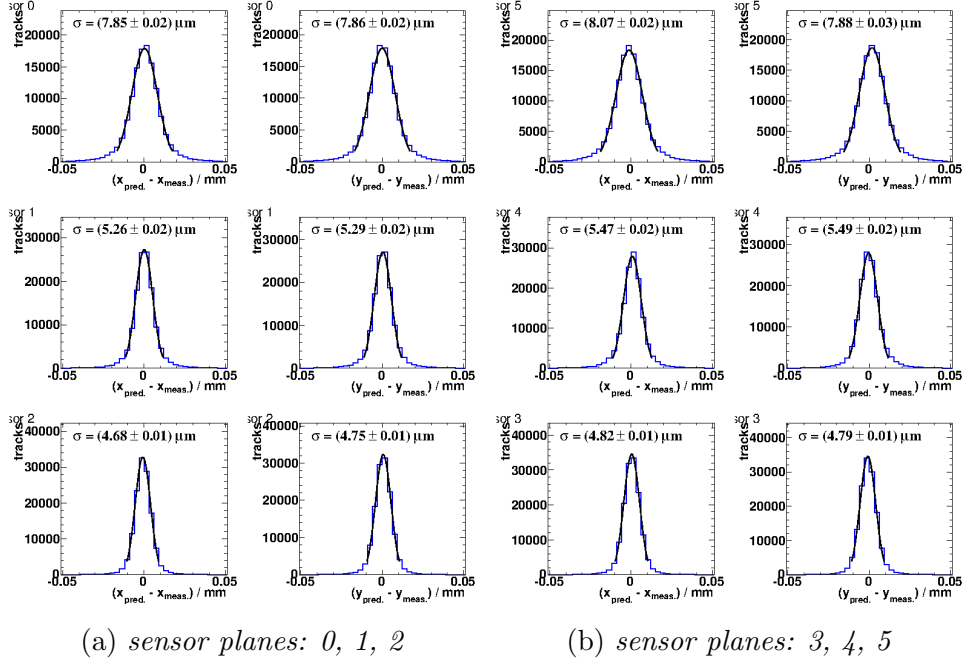


Figure 21: *Residuals distributions for threshold 5 and beam energy 2 GeV*

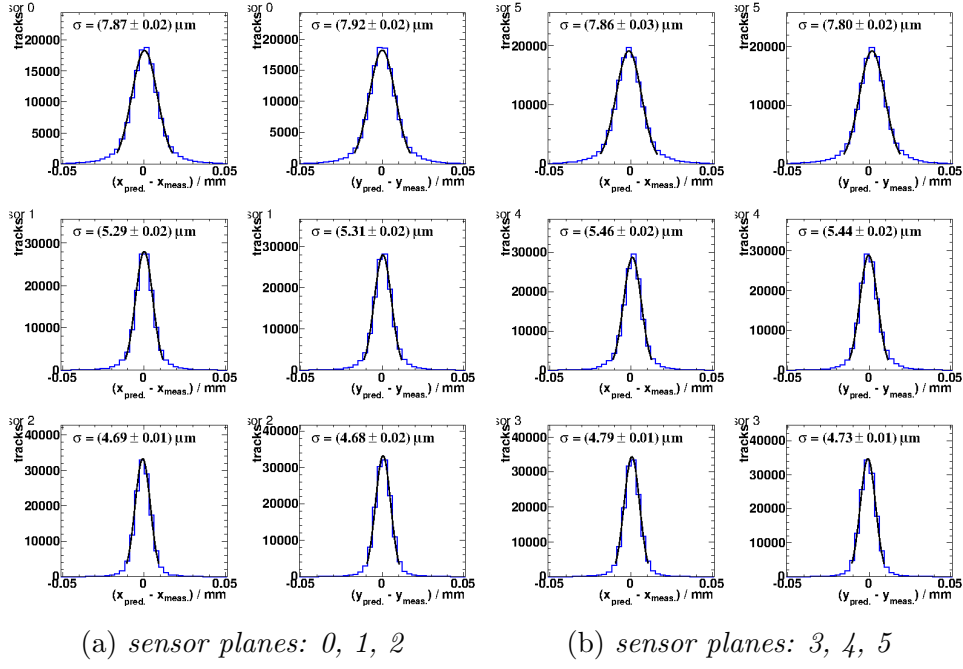


Figure 22: *Residuals distributions for threshold 6 and beam energy 2 GeV*

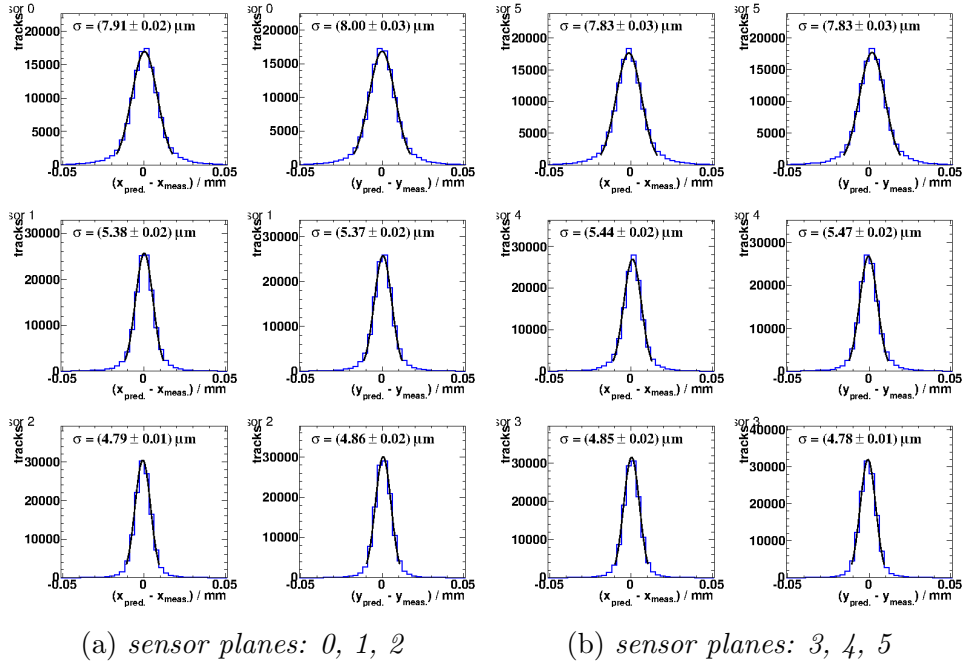


Figure 23: *Residuals distributions for threshold 7 and beam energy 2 GeV*

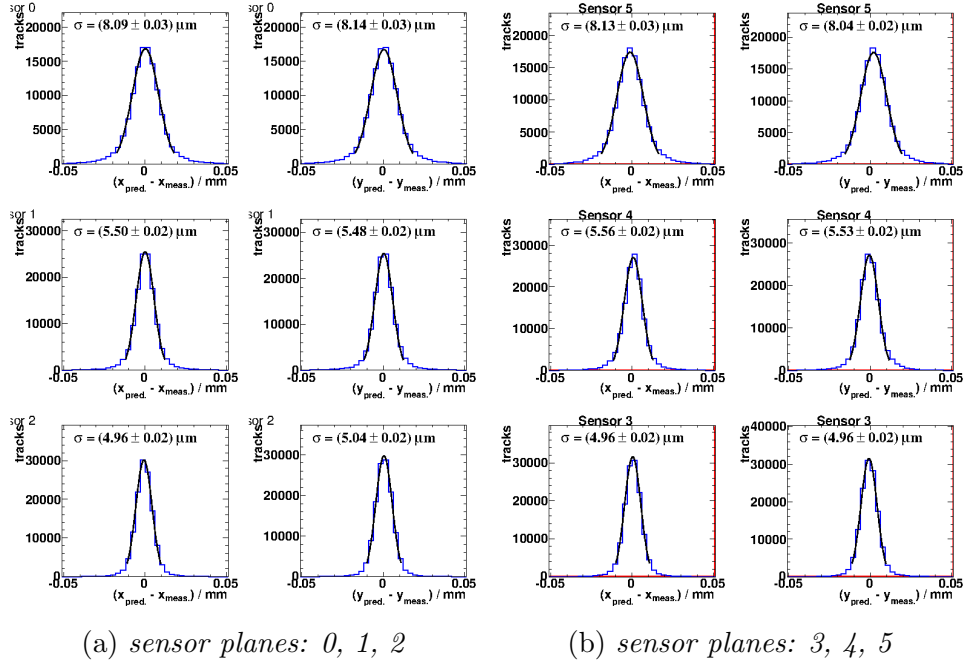


Figure 24: *Residuals distributions for threshold 8 and beam energy 2 GeV*

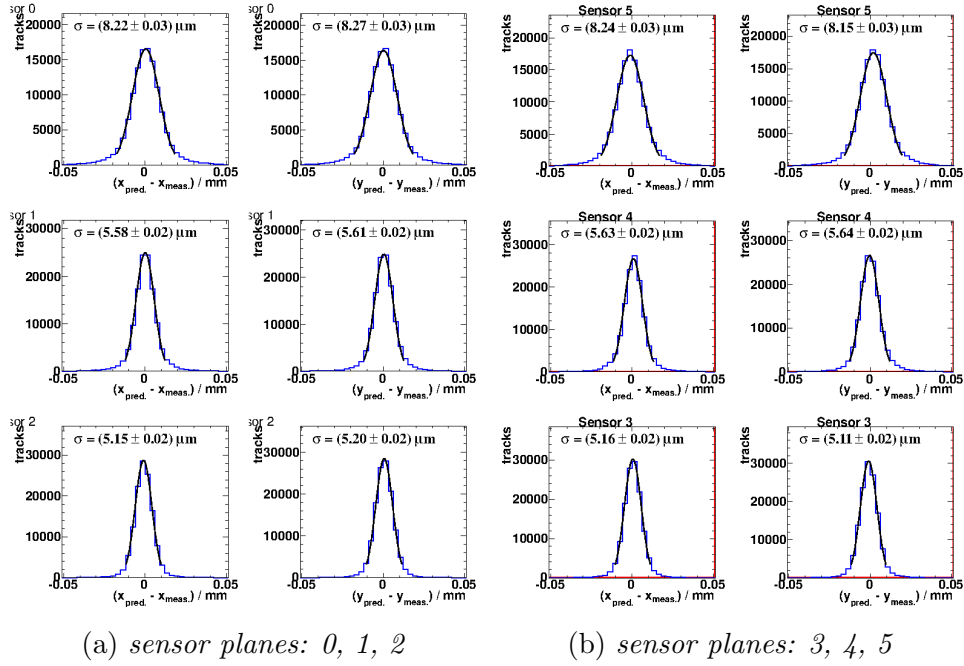


Figure 25: *Residuals distributions for threshold 9 and beam energy 2 GeV*



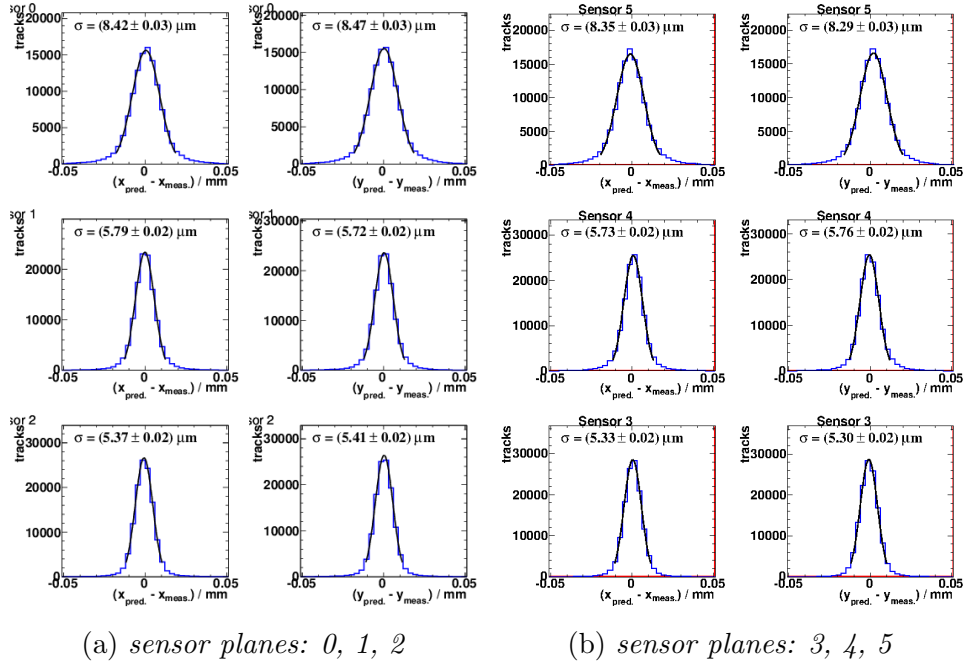


Figure 26: Residuals distributions for threshold 10 and beam energy 2 GeV

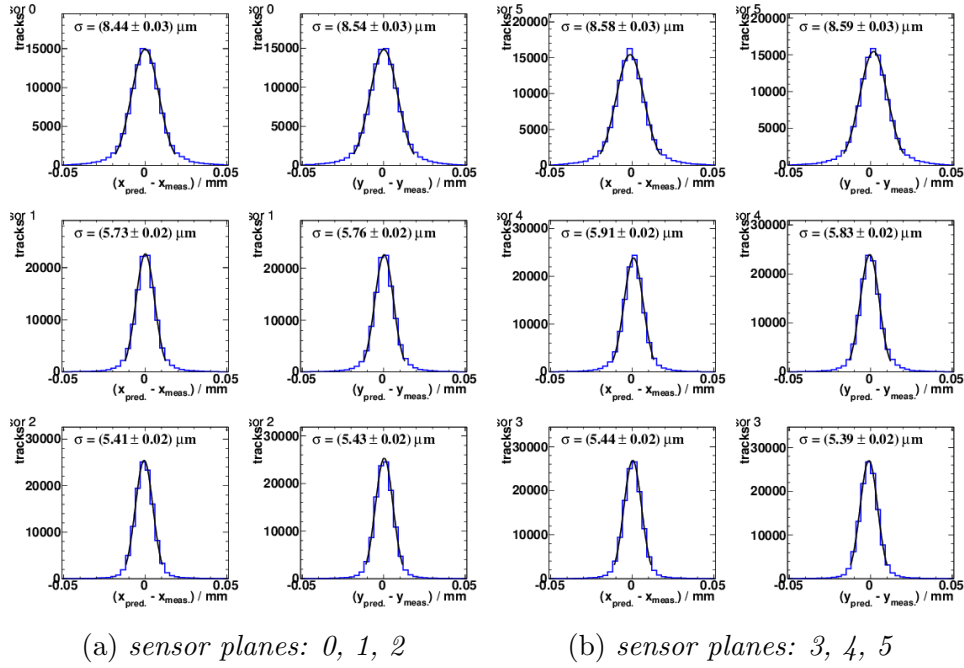


Figure 27: Residuals distributions for threshold 11 and beam energy 2 GeV

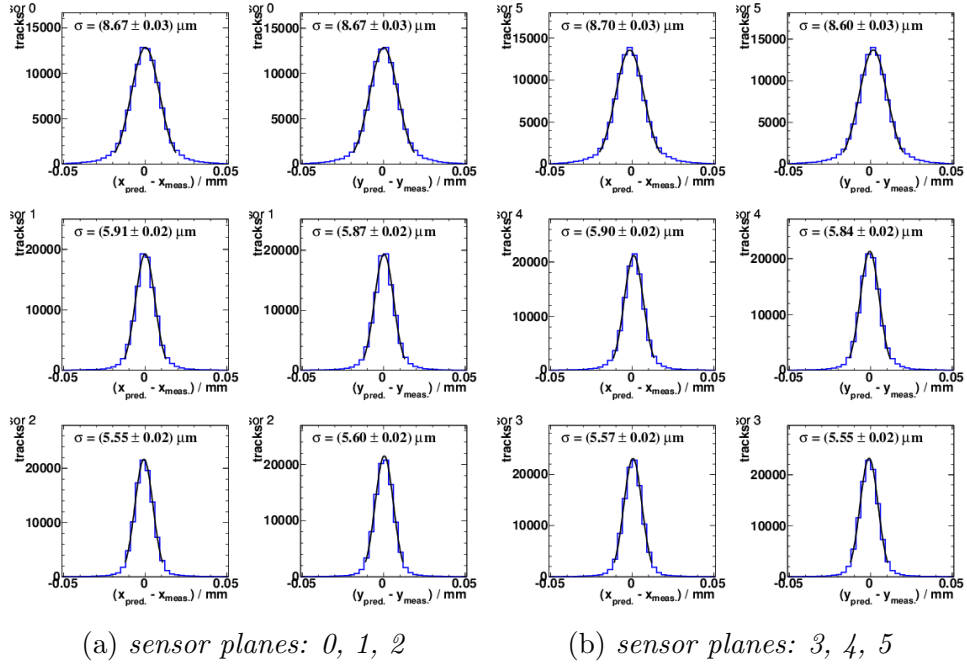


Figure 28: *Residuals distributions for threshold 12 and beam energy 2 GeV*

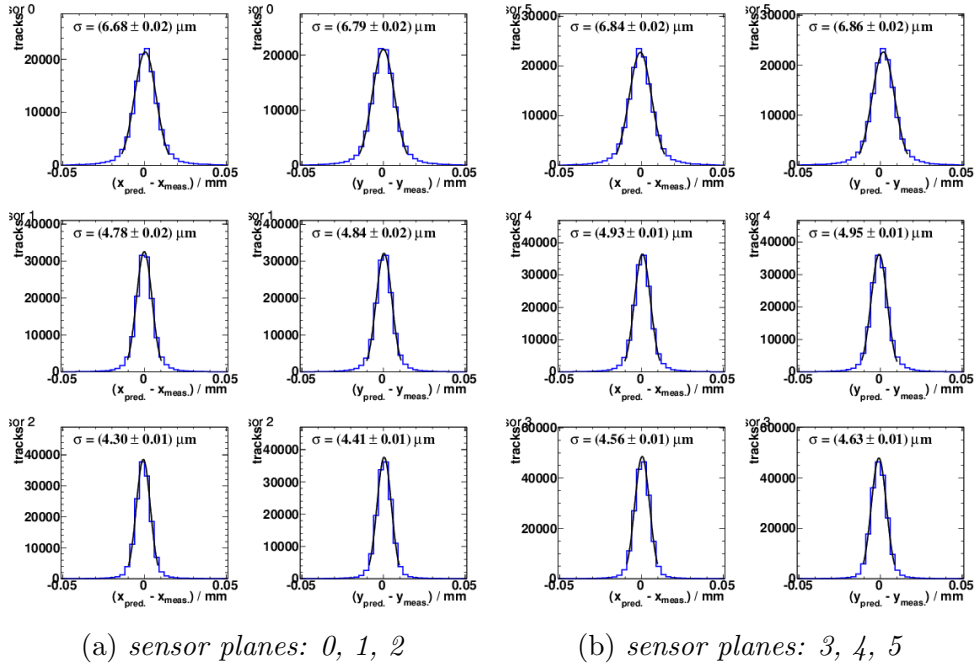


Figure 29: *Residuals distributions for threshold 3 and beam energy 3 GeV*

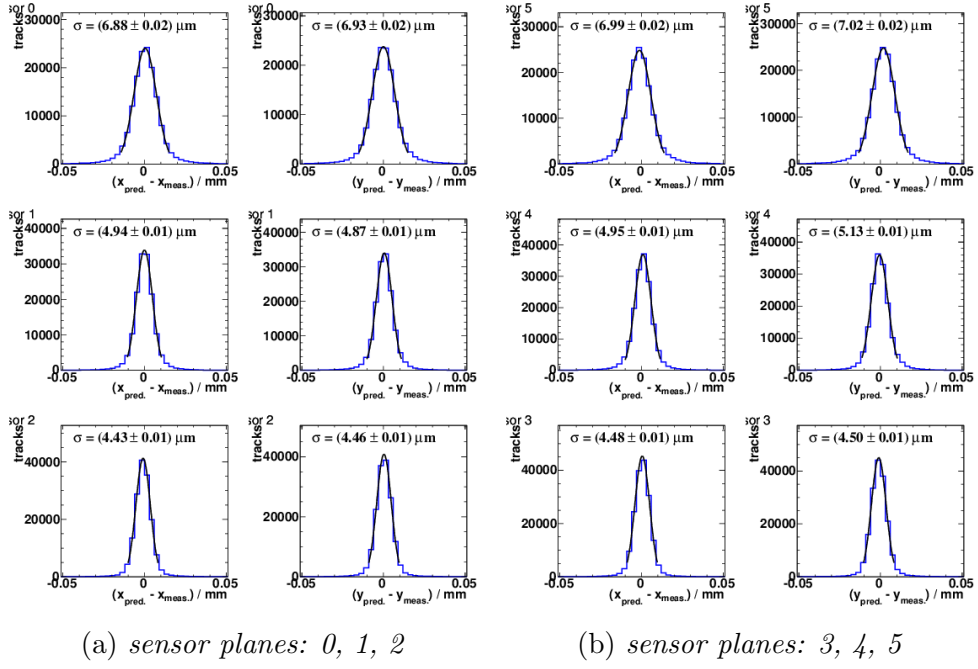


Figure 30: *Residuals distributions for threshold 4 and beam energy 3 GeV*

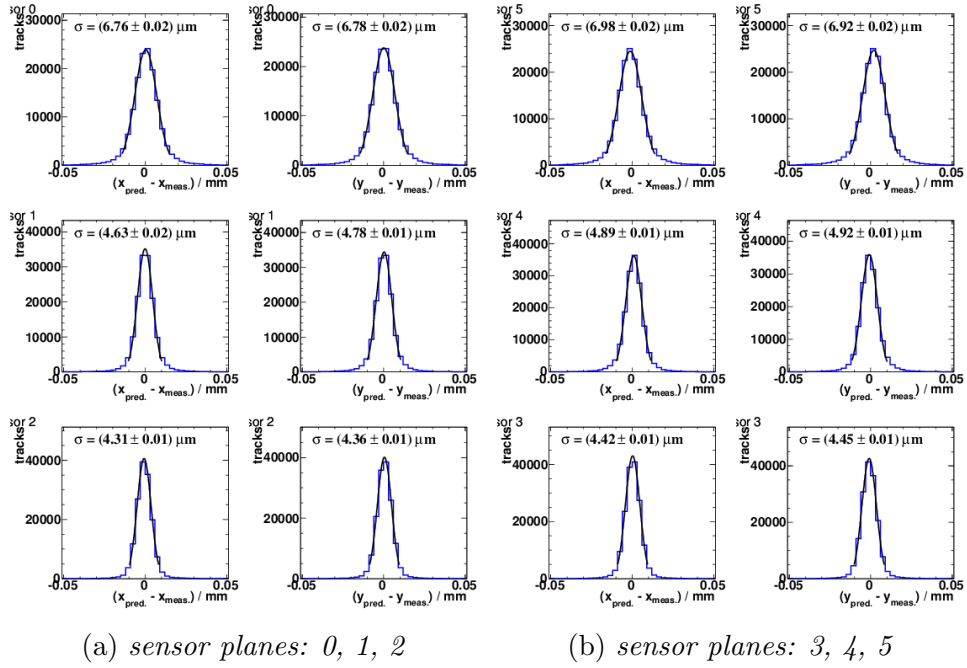


Figure 31: *Residuals distributions for threshold 5 and beam energy 3 GeV*

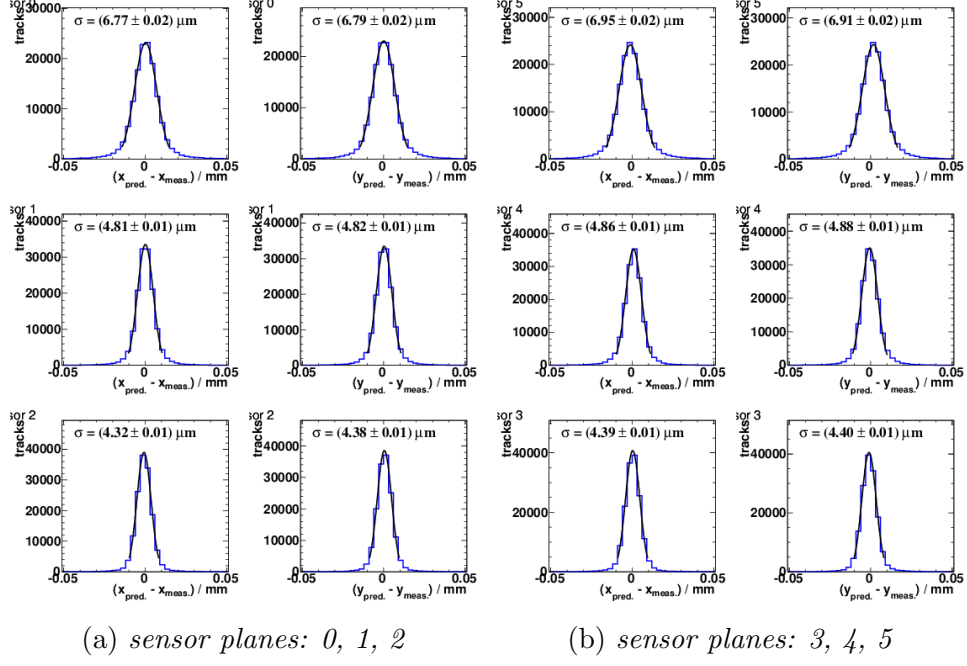


Figure 32: *Residuals distributions for threshold 6 and beam energy 3 GeV*

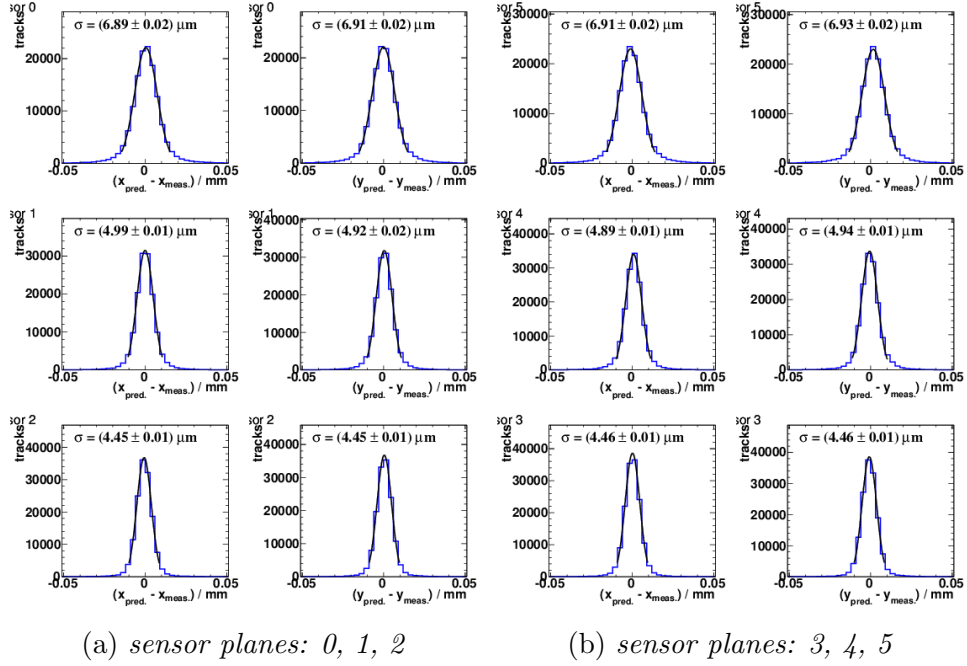


Figure 33: *Residuals distributions for threshold 7 and beam energy 3 GeV*

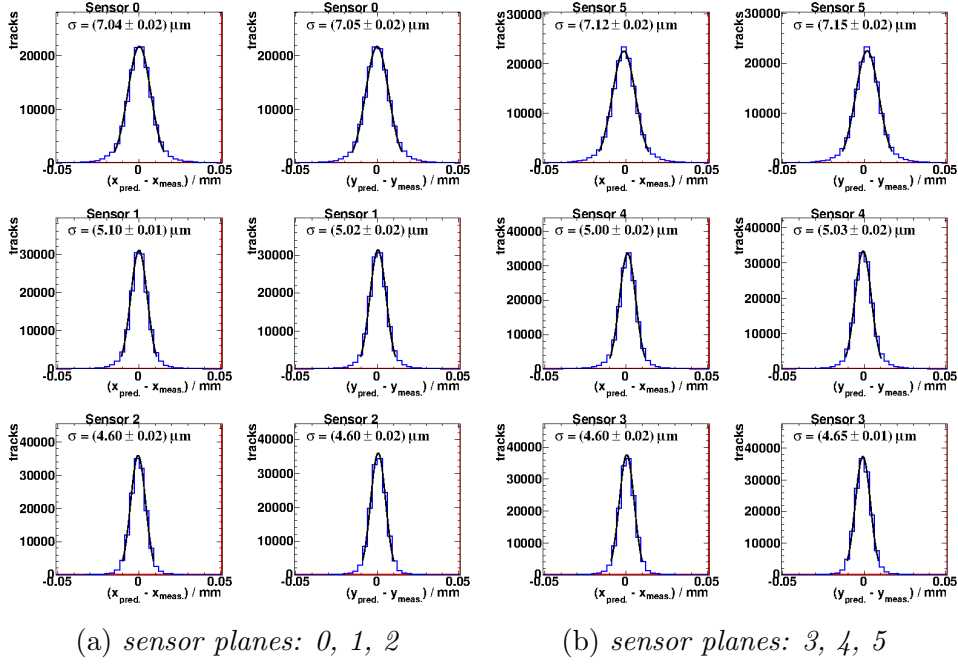


Figure 34: *Residuals distributions for threshold 8 and beam energy 3 GeV*

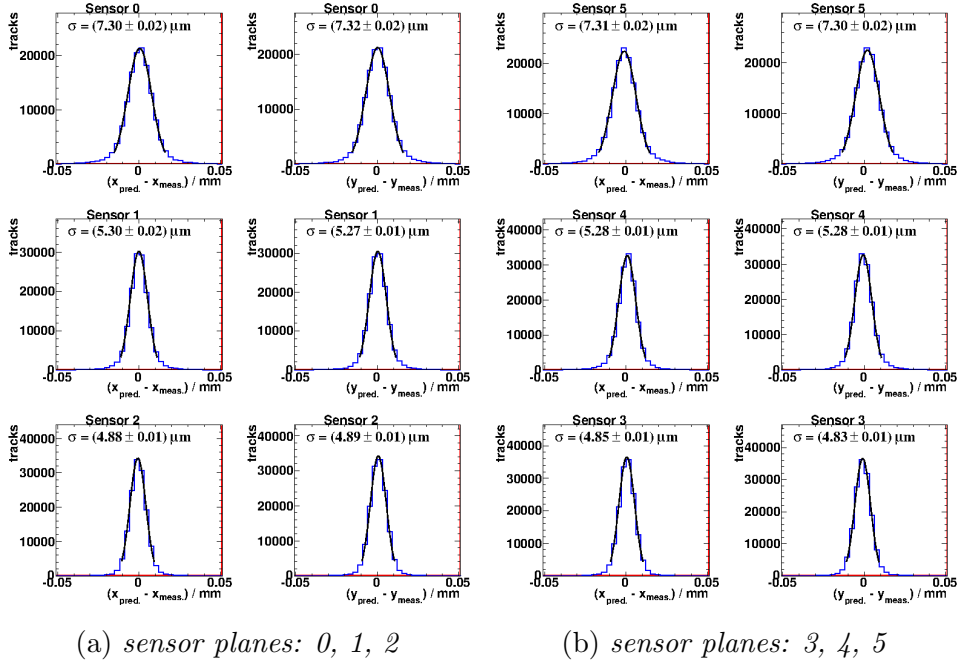


Figure 35: *Residuals distributions for threshold 9 and beam energy 3 GeV*

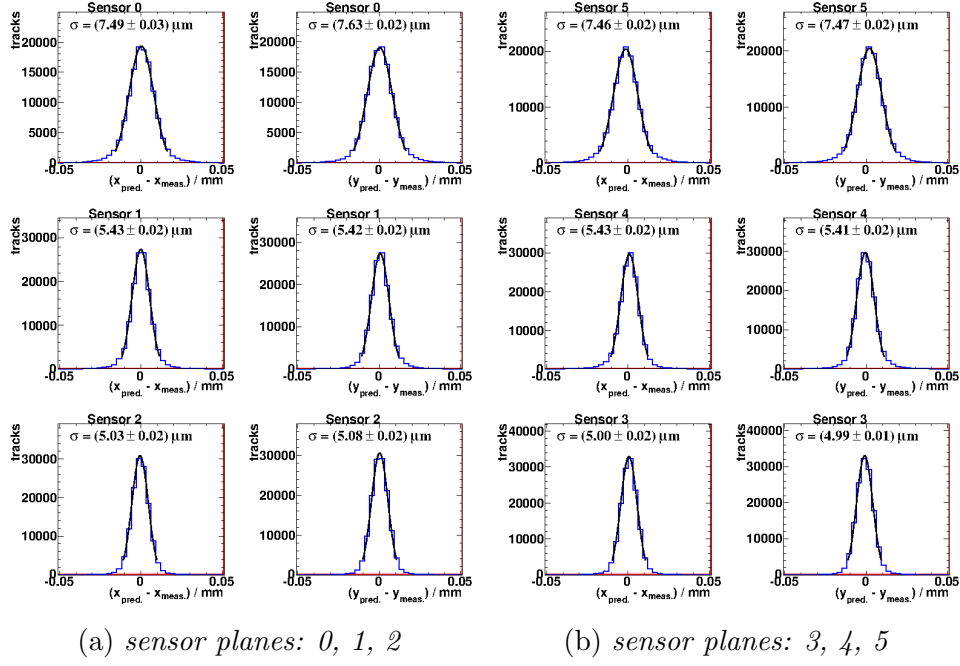


Figure 36: *Residuals distributions for threshold 10 and beam energy 3 GeV*

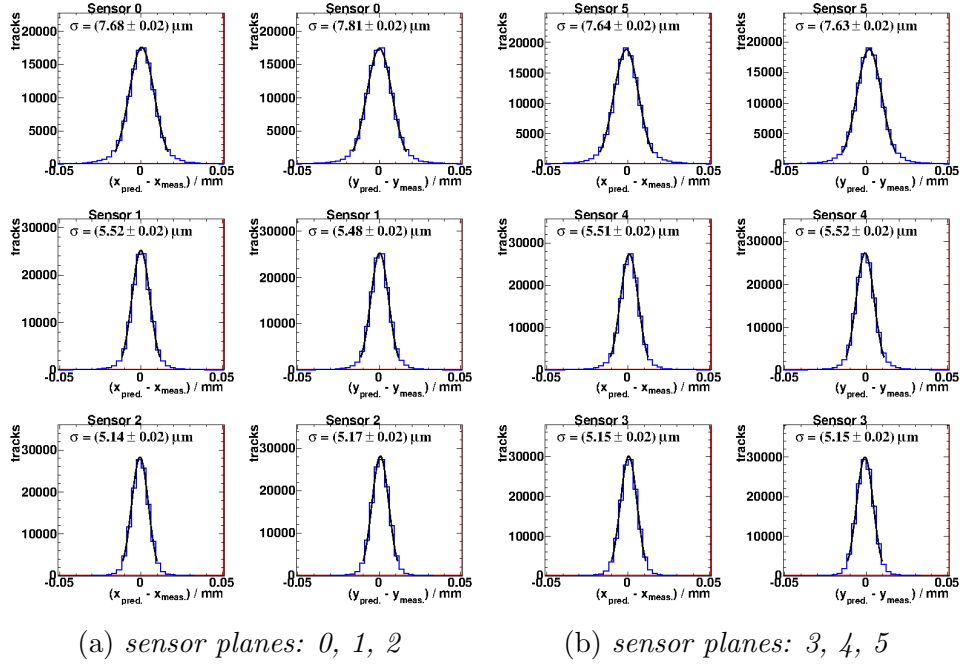


Figure 37: *Residuals distributions for threshold 11 and beam energy 3 GeV*

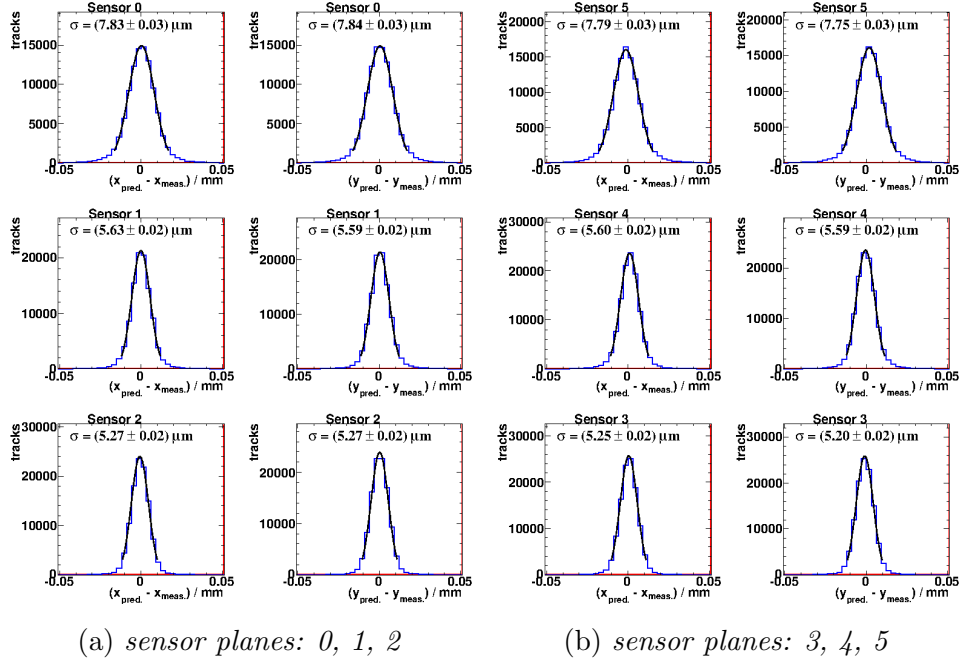


Figure 38: *Residuals distributions for threshold 12 and beam energy 3 GeV*

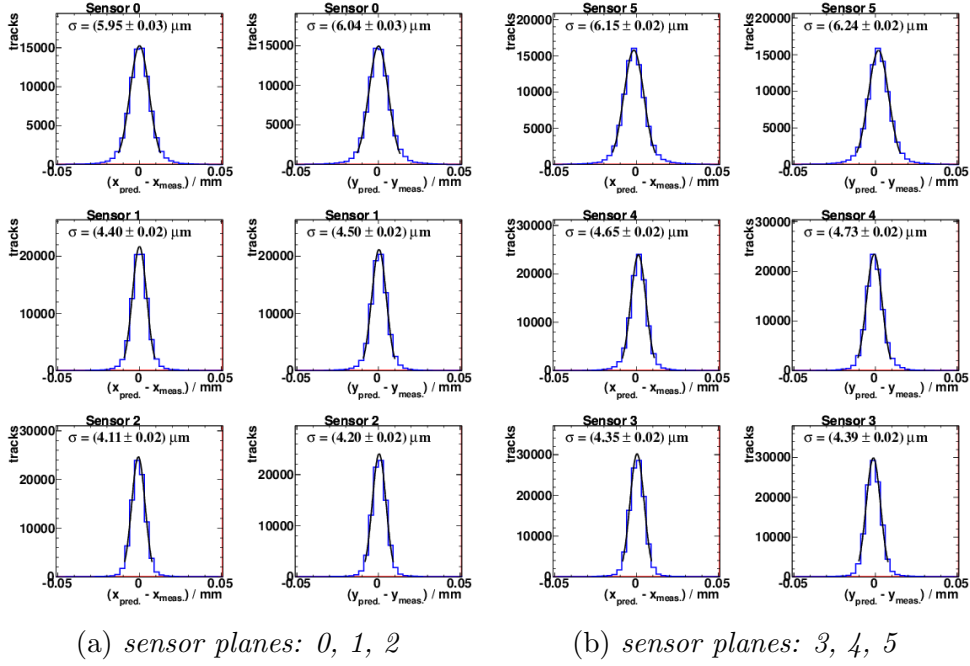


Figure 39: *Residuals distributions for threshold 3 and beam energy 5 GeV*



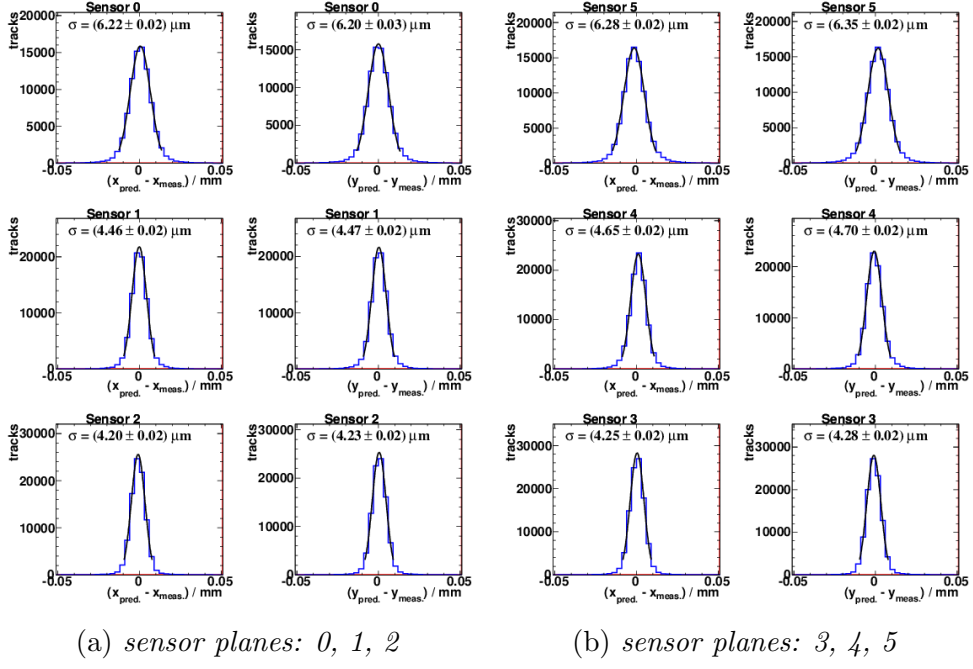


Figure 40: *Residuals distributions for threshold 4 and beam energy 5 GeV*

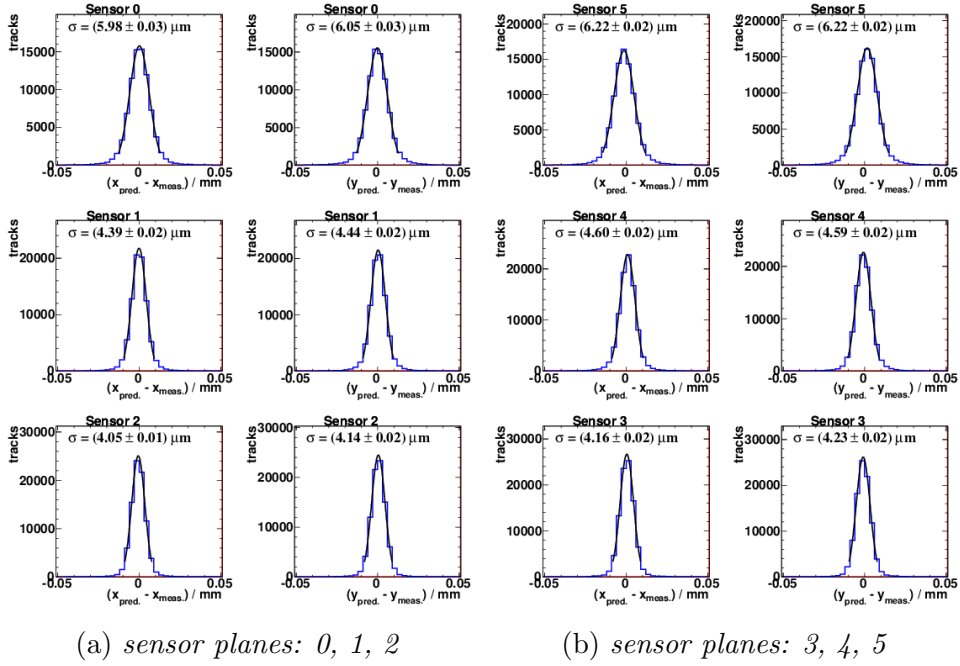


Figure 41: *Residuals distributions for threshold 5 and beam energy 5 GeV*

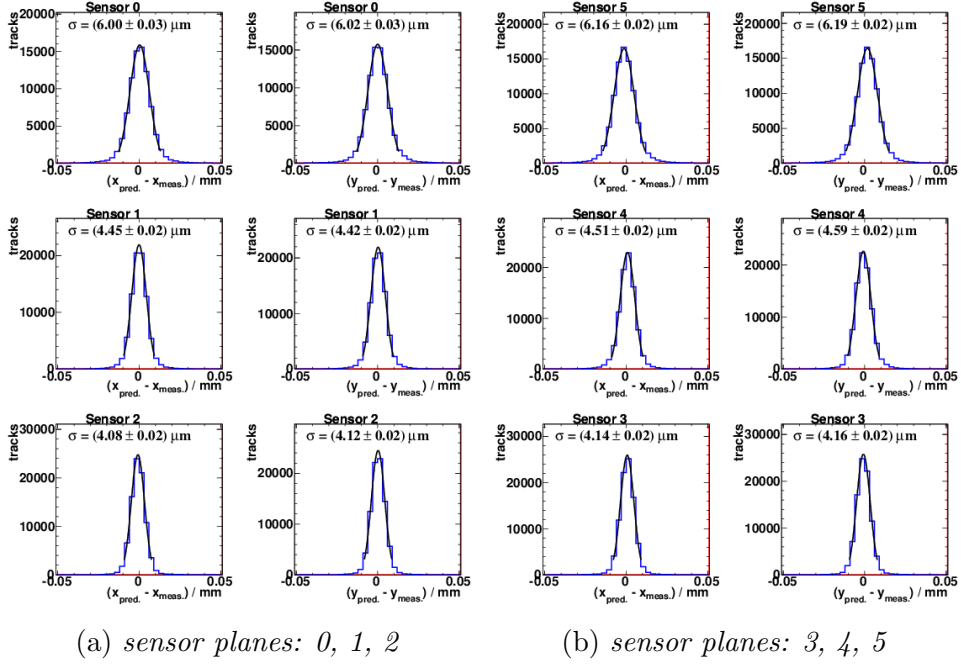


Figure 42: *Residuals distributions for threshold 6 and beam energy 5 GeV*

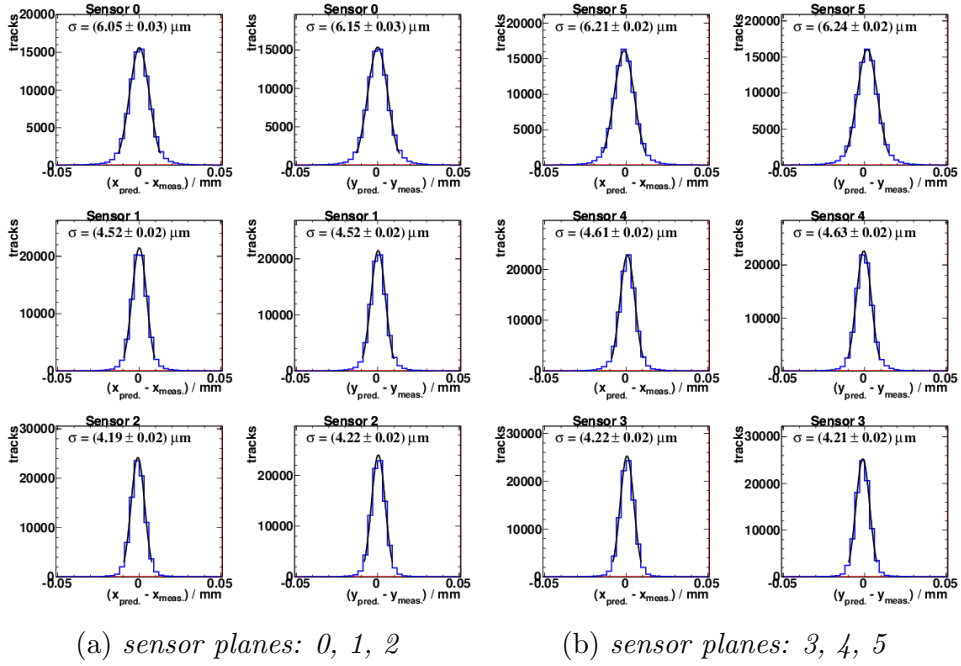


Figure 43: *Residuals distributions for threshold 7 and beam energy 5 GeV*

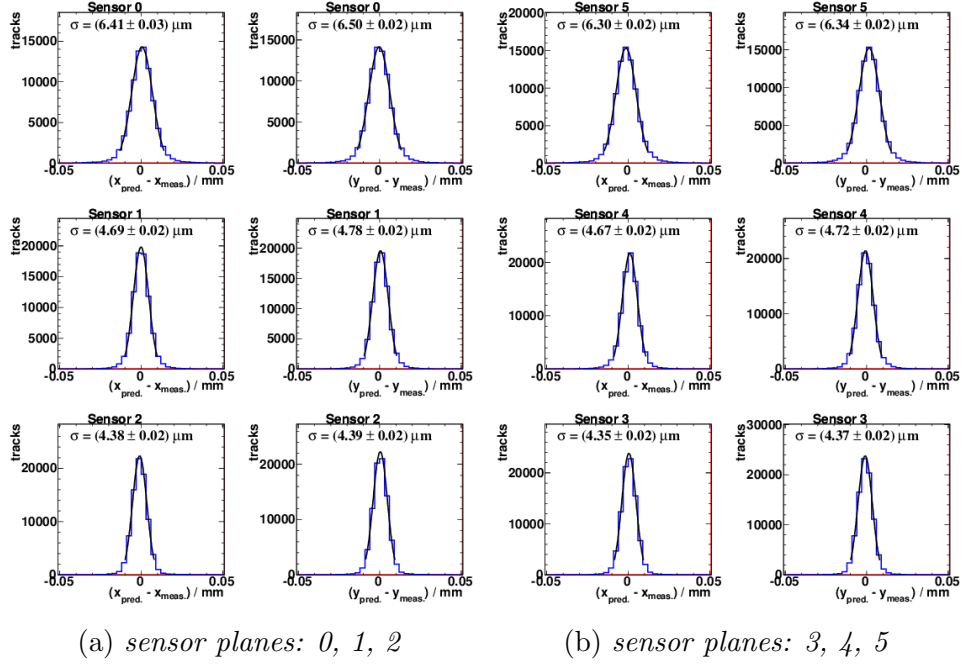


Figure 44: *Residuals distributions for threshold 8 and beam energy 5 GeV*

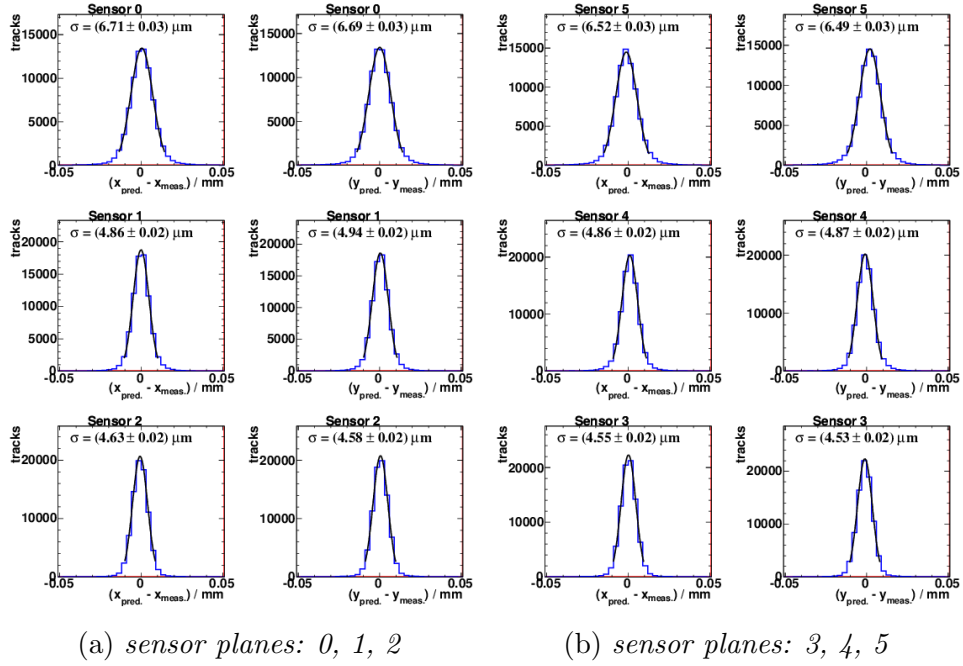


Figure 45: *Residuals distributions for threshold 9 and beam energy 5 GeV*

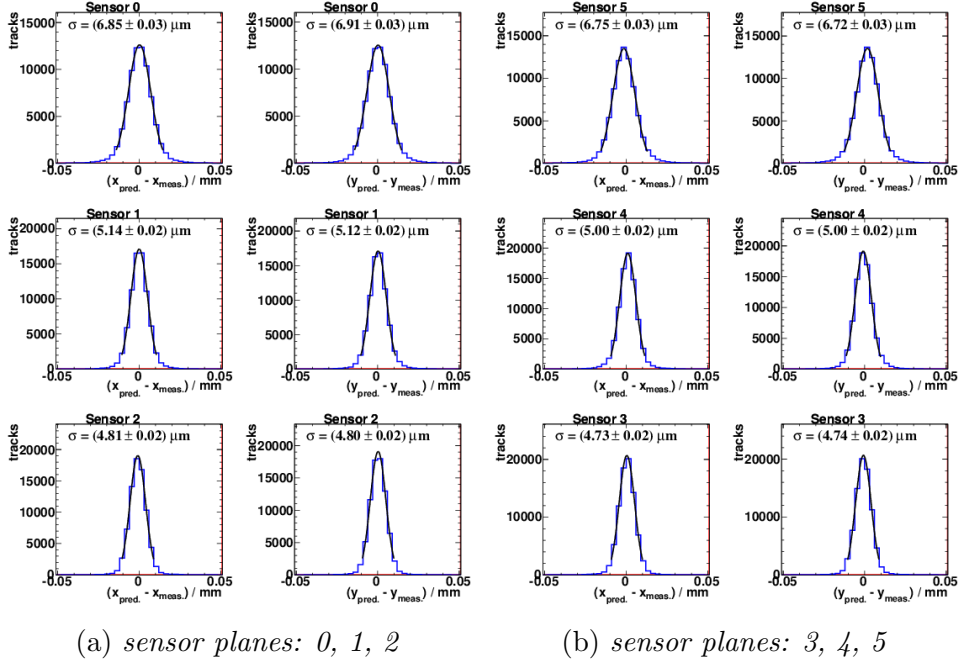


Figure 46: *Residuals distributions for threshold 10 and beam energy 5 GeV*

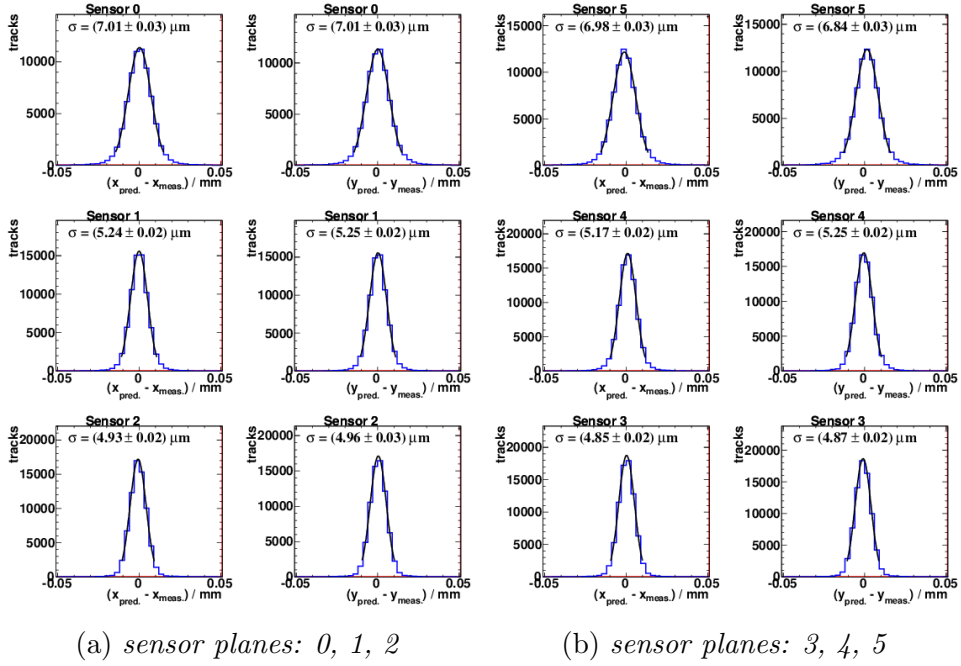


Figure 47: *Residuals distributions for threshold 11 and beam energy 5 GeV*

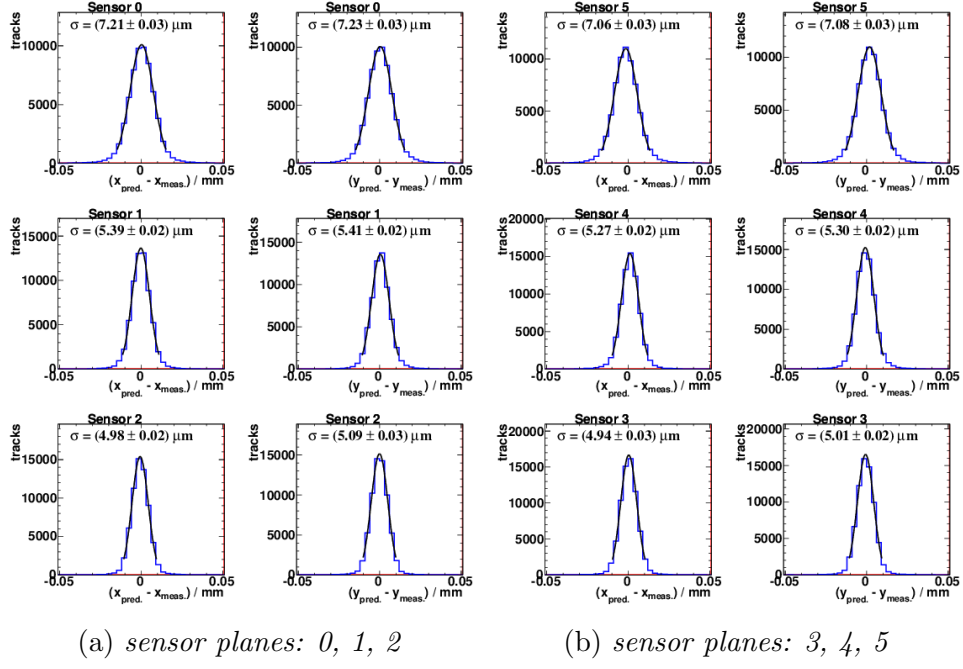


Figure 48: *Residuals distributions for threshold 12 and beam energy 5 GeV*

## B Fitted widths of unbiased residuals

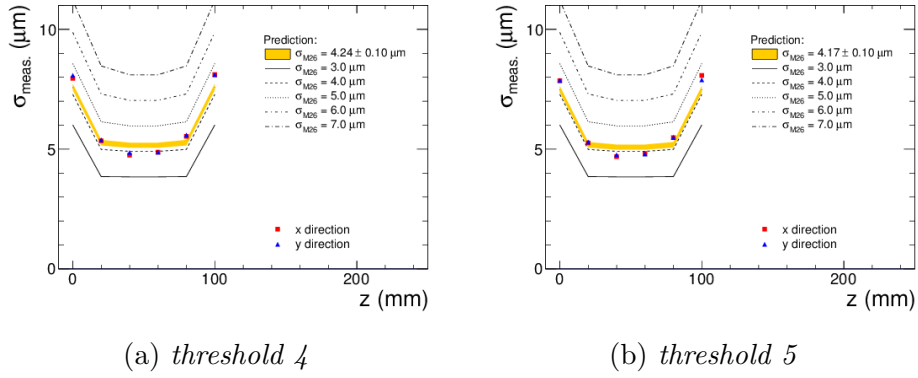
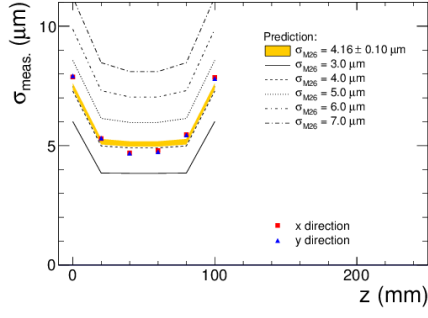
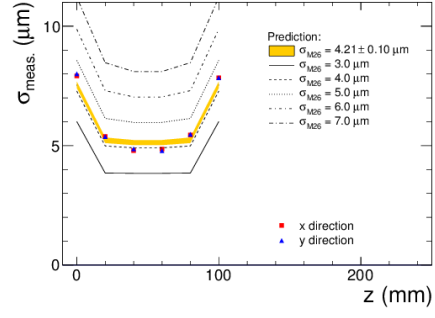


Figure 49: *Fitted widths of the unbiased residuals as a function of distance, beam energy 2 GeV.*

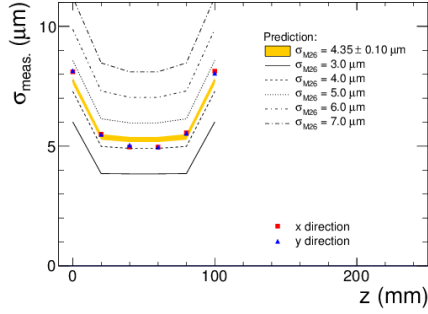


(a) threshold 6

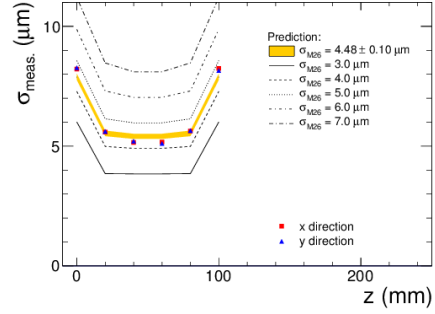


(b) threshold 7

Figure 50: *Fitted widths of the unbiased residuals as a function of distance, beam energy 2 GeV.*

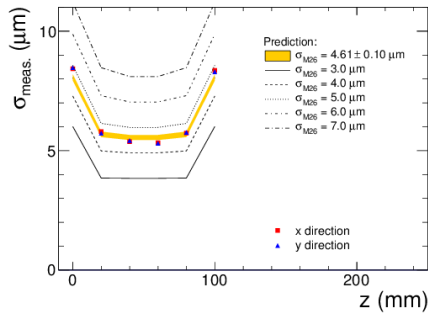


(a) threshold 8

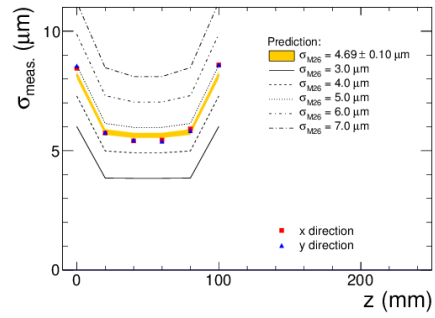


(b) threshold 9

Figure 51: *Fitted widths of the unbiased residuals as a function of distance, beam energy 2 GeV.*

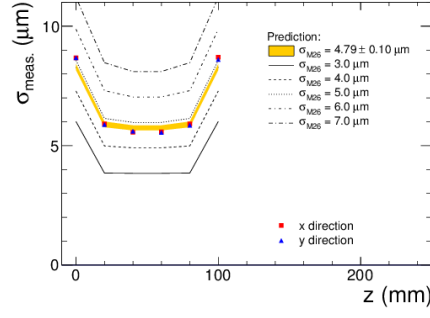


(a) threshold 10



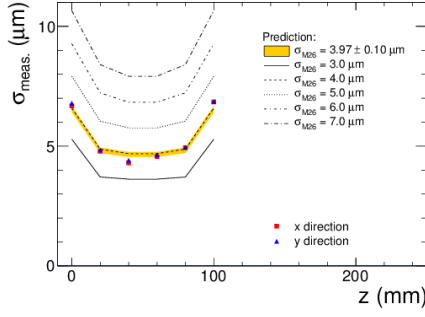
(b) threshold 11

Figure 52: *Fitted widths of the unbiased residuals as a function of distance, beam energy 2 GeV.*

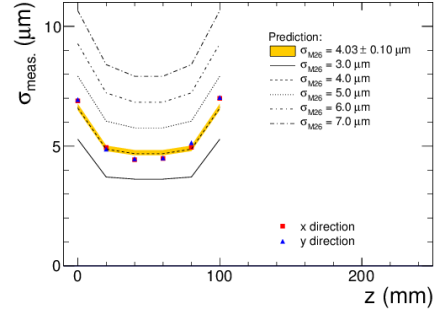


(a) threshold 12

Figure 53: *Fitted widths of the unbiased residuals as a function of distance, beam energy 2 GeV.*

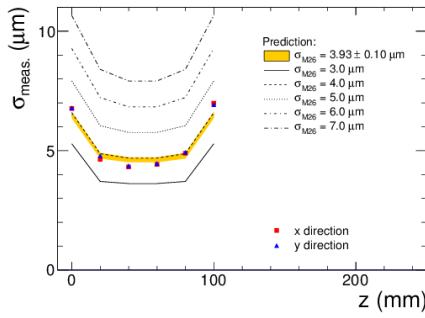


(a) threshold 3

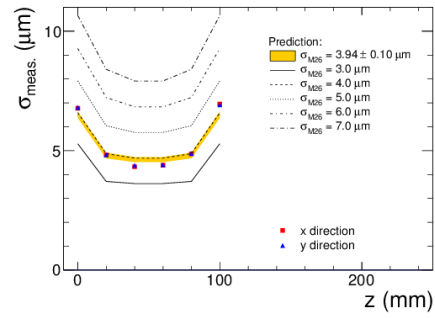


(b) threshold 4

Figure 54: *Fitted widths of the unbiased residuals as a function of distance, beam energy 3 GeV.*

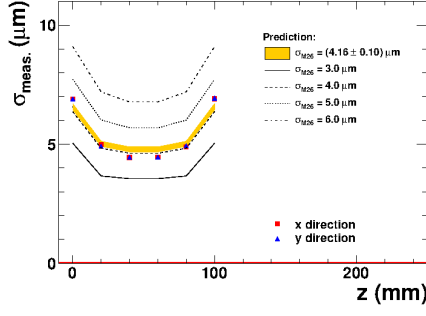


(a) threshold 5

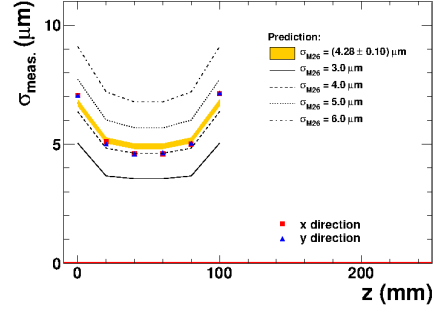


(b) threshold 6

Figure 55: *Fitted widths of the unbiased residuals as a function of distance, beam energy 3 GeV.*

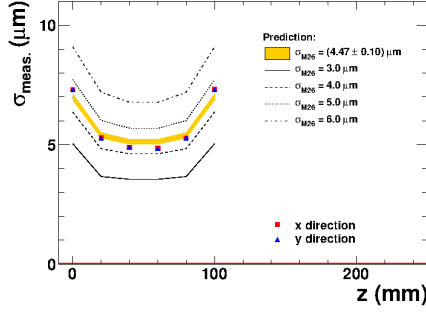


(a) threshold 7

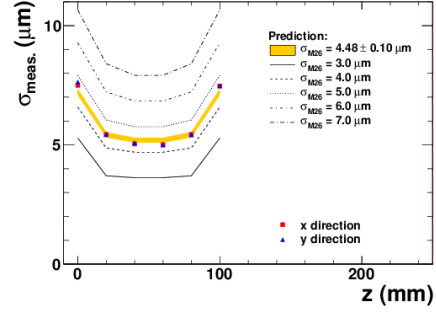


(b) threshold 8

Figure 56: *Fitted widths of the unbiased residuals as a function of distance, beam energy 3 GeV.*

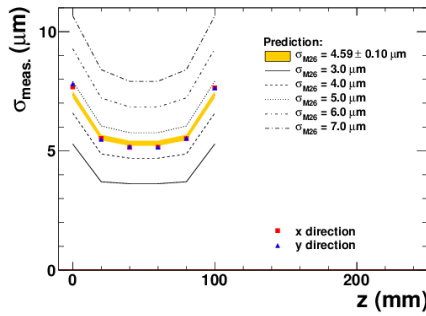


(a) threshold 9

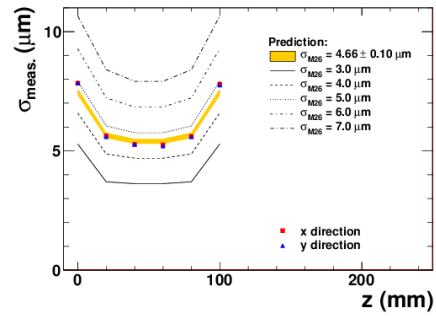


(b) threshold 10

Figure 57: *Fitted widths of the unbiased residuals as a function of distance, beam energy 3 GeV.*



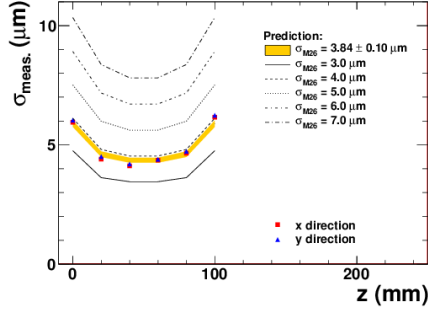
(a) threshold 11



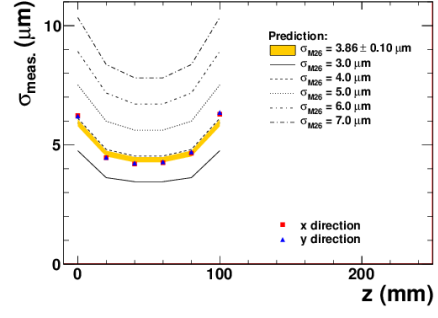
(b) threshold 12

Figure 58: *Fitted widths of the unbiased residuals as a function of distance, beam energy 3 GeV.*



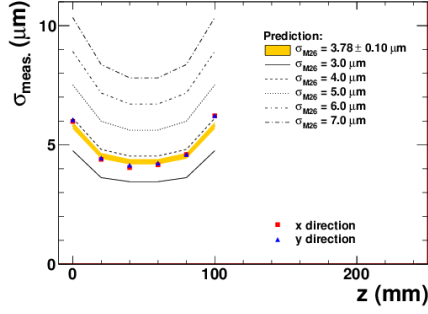


(a) threshold 3

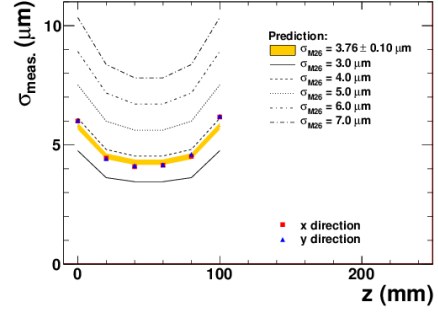


(b) threshold 4

Figure 59: *Fitted widths of the unbiased residuals as a function of distance, beam energy 5 GeV.*

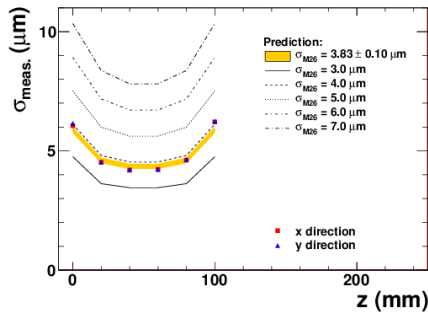


(a) threshold 5

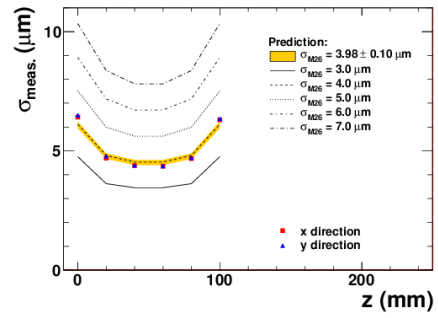


(b) threshold 6

Figure 60: *Fitted widths of the unbiased residuals as a function of distance, beam energy 5 GeV.*

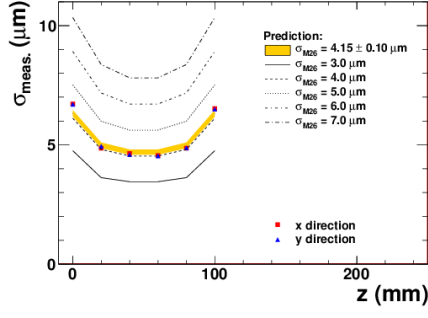


(a) threshold 7

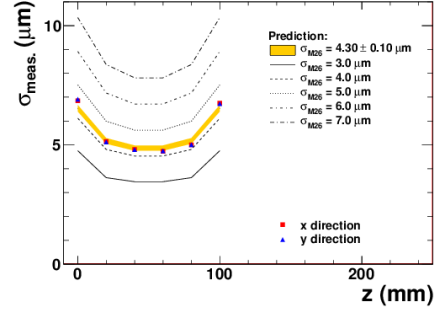


(b) threshold 8

Figure 61: *Fitted widths of the unbiased residuals as a function of distance, beam energy 5 GeV.*

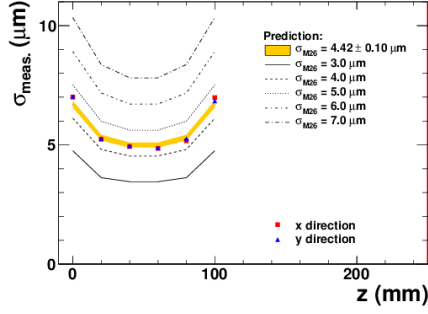


(a) threshold 9

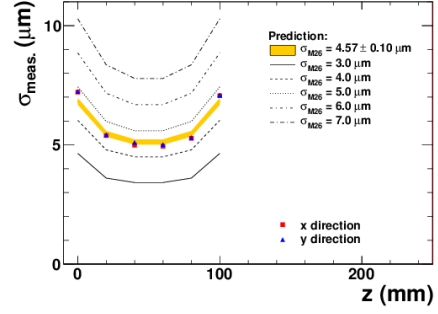


(b) threshold 10

Figure 62: Fitted widths of the unbiased residuals as a function of distance, beam energy 5 GeV.



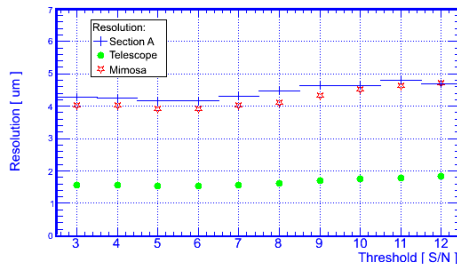
(a) threshold 11



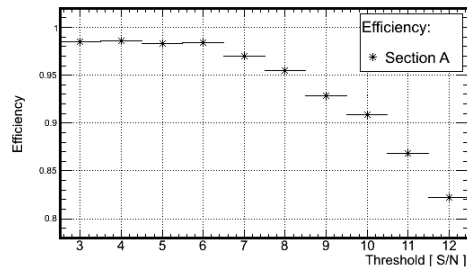
(b) threshold 12

Figure 63: Fitted widths of the unbiased residuals as a function of distance, beam energy 5 GeV.

## C Efficiency and resolution plots

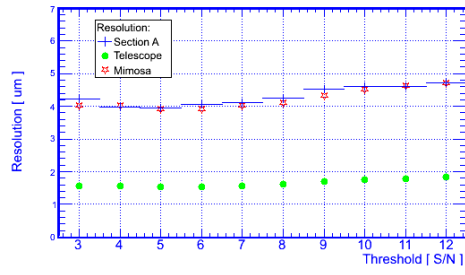


(a) Resolutions

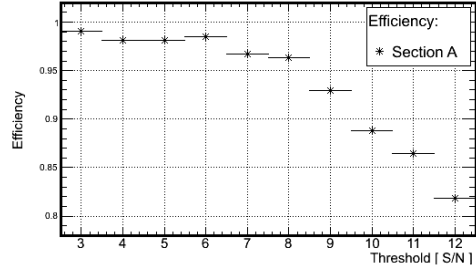


(b) Efficiency

Figure 64: Sensor no. 76 (plane 2), beam energy 3 GeV



(a) *Resolutions*



(b) *Efficiency*

Figure 65: *Sensor no. 76 (plane 2), beam energy 5 GeV*